DESIGN AND CHARACTERIZATION OF A ROBUST MEMS MEMBRANE
UNDER RESIDUAL STRESS

A THESIS SUBMITTED TO
THE GRADUATE SCHOOL OF NATURAL AND APPLIED SCIENCES
OF
MIDDLE EAST TECHNICAL UNIVERSITY

BY

MUSTAFA ANIL BOZYİĞİT

IN PARTIAL FULFILLMENT OF THE REQUIREMENTS
FOR
THE DEGREE OF MASTER OF SCIENCE
IN
ELECTRICAL AND ELECTRONICS ENGINEERING

JANUARY 2020

Approval of the thesis:

DESIGN AND CHARACTERIZATION OF A ROBUST MEMS MEMBRANE UNDER RESIDUAL STRESS

submitted by **MUSTAFA ANIL BOZYIĞIT** in partial fulfillment of the requirements for the degree of **Master of Science in Electrical and Electronics Engineering Department, Middle East Technical University** by,

Prof. Dr. Halil Kalıpçılar
Dean, Graduate School of **Natural and Applied Sciences**   _____

Prof. Dr. İlkay Ulusoy
Head of Department, **Electrical and Electronics Eng.**   _____

Prof. Dr. Barış Bayram
Supervisor, **Electrical and Electronics Eng., METU**   _____

Examining Committee Members:

Prof. Dr. Tayfun Akın
Electrical and Electronics Eng., METU   _____

Prof. Dr. Barış Bayram
Electrical and Electronics Eng., METU   _____

Prof. Dr. Murat Eyüboğlu
Electrical and Electronics Eng., METU   _____

Prof. Dr. Hayrettin Köymen
Electrical and Electronics Eng., Bilkent University   _____

Assoc. Prof. Dr. Serdar Kocaman
Electrical and Electronics Eng., METU   _____

Date: 30.01.2020

I hereby declare that all information in this document has been obtained and presented in accordance with academic rules and ethical conduct. I also declare that, as required by these rules and conduct, I have fully cited and referenced all material and results that are not original to this work.

Name, Surname: Mustafa Anıl Bozyiğit

Signature:

ABSTRACT

**DESIGN AND CHARACTERIZATION OF A ROBUST MEMS MEMBRANE
UNDER RESIDUAL STRESS**

Bozyiğit, Mustafa Anıl
Master of Science, Electrical and Electronics Engineering
Supervisor: Prof. Dr. Barış Bayram

January 2020, 73 pages

MEMS membranes are utilized as both transmitter and receiver in acoustic and ultrasound applications. Their operating frequency ranges are determined by their resonance frequencies. Thus, the resonance frequency estimation is one of the most critical part of the membrane design. In this study, two perforated circular MEMS membranes are designed and fabricated with PolyMUMPs process. The radius values are chosen as 220 μm and 205 μm to get proper operation under residual stress since this stress might cause buckling of the membrane. Finite element methods (FEM) and optical measurements are performed to extract the resonance frequencies. For the fundamental mode, the FEM results deviate 5.5% and 6.7% from the experimental work. Also, critical stress parameters of the membranes are investigated with finite element analysis. 33.4% stress relaxation is achieved for the proposed perforated membranes. Furthermore, eight different circular membranes are simulated and compared with the analytical solutions. The minimum and maximum average errors are acquired as 0.5% and 3.3% for the fundamental mode. The electrical characterizations are carried out with the impedance analyzer and results are supported by FEM. Stress was successfully managed with the help of the perforation, as verified by the experimental work and simulations.

ÖZ

KALINTI GERİLİMİ ALTINDA DAYANIKLI MEMS DİYAFRAMLARIN TASARIMI VE KARAKTERİZASYONU

Bozyiğit, Mustafa Anıl
Yüksek Lisans, Elektrik ve Elektronik Mühendisliği
Tez Danışmanı: Prof. Dr. Barış Bayram

Ocak 2020, 73 sayfa

MEMS diyaframları akustik ve ultrason uygulamalarında hem verici hem de alıcı olarak kullanılır. Çalışma frekans aralıkları rezonans frekanslarına göre belirlenir. Bu nedenle, rezonans frekans tahmini diyafram tasarımının en kritik kısımlarından biridir. Bu çalışmada, iki delikli dairesel MEMS diyaframı PolyMUMPs işlemi ile tasarlanmış ve imal edilmiştir. Yarıçap değerleri, kalıntı stres altında düzgün çalışmayı sağlamak için 220 um ve 205 um olarak seçilir, çünkü bu stres diyaframın burkulmasına neden olabilir. Rezonans frekanslarını çıkarmak için sonlu elemanlar yöntemi (FEM) ve optik ölçümler yapılır. Temel mod için, FEM sonuçları deneysel çalışmadan %5.5 ve %6.7 sapmaktadır. Ayrıca, diyaframların kritik gerilim parametreleri sonlu elemanlar analizi ile araştırılmaktadır. Önerilen delikli diyaframlar için %33.4 gerilim gevşemesi sağlanır. Ayrıca, sekiz farklı dairesel diyafram simüle edilir ve analitik çözümlerle karşılaştırılır. Minimum ve maksimum ortalama hataları temel mod için %0,5 ve %3,3 olarak elde edilir. Elektriksel özellikler empedans analizörü ile gerçekleştirilir ve sonuçlar FEM tarafından desteklenir. Stres, deneysel çalışmalar ve simülasyonlarla doğrulandığı gibi, delikler yardımıyla başarıyla yönetildi.

Anahtar Kelimeler: Kalıntı Stresi, Kritik Eğilme, Delikli Diyafram

To my family

ACKNOWLEDGEMENTS

TABLE OF CONTENTS

LIST OF TABLES

LIST OF FIGURES

FIGURES

CHAPTER 1

INTRODUCTION

1.1. Microelectromechanical Systems

Microelectromechanical systems (MEMS) are the integrated structures that consist of the electrical and mechanical components in microscales. Their fabrication processes are similar with the development procedures of Integrated Circuits (IC). Under favor of this correlation, MEMS devices may be fabricated in a single substrate with IC technologies. They can mimic the macro scale devices to sense the environmental changes.

MEMS arise from the interdisciplinary studies such as mechanical engineering, electrical engineering, chemical engineering, material sciences. Through the involvement of the different scientific approaches, the MEMS devices have wide range application area like pressure sensors, accelerometers, optical switches, microphones, biosensors and many other products. Thus, they have high commercial volumes in market [1].

Depending on the application area, the MEMS devices may be composed of simple non-moving structures or highly complex multiple moving mechanical systems. The defined mission of the MEMS device determines the complexity of the structures. However, the development of the complex structures is based on the advanced fabrication techniques.

1.2. Fabrication Methods

1.2.1. Bulk Micromachining

The MEMS devices are formed with the etching processes in bulk micromachining. The basic principle of the bulk micromachining is the removal of the

unwanted parts on the bulk substrate. For this purpose, dry or wet etching processes are used in bulk micromachining [1].

In wet etching, the materials are immersed into the chemical etchants. It consists of two types of etching which are anisotropic and isotropic etching. The etching rate is the same for all directions in isotropic etching. Hence, it also removes the materials under the etch mask which is called as undercutting. On the other hand, the anisotropic etching has directional sensitivity. The etching rates change with the crystal orientation. Thus, structures are formed depending on their orientations [2]. The isotropic and anisotropic etching examples are shown in Figure 1.1.
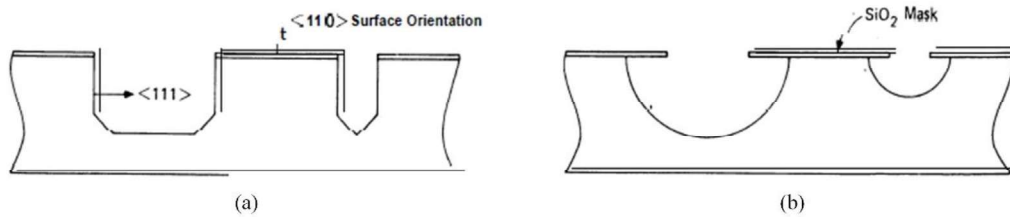
Figure 1.1. (a) Anisotropic etching, (b) Isotropic etching example [2]

The etching materials are transferred to vapor or plasma phases for the dry etching. Furthermore, accelerated ions are used with the reactive vapors. The ions provide additional energy to handle etching reactions. The most common dry etching method is Reactive Ion Etching (RIE). The reactive plasma is generated by electromagnetic field, and it is directed to the surface. The highly energetic ions are performed the etching process by forming deep trenches [3].
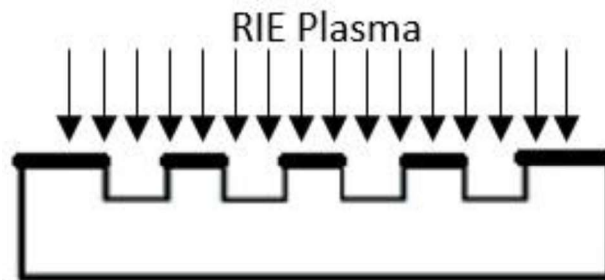
Figure 1.2. Obtained structure after RIE etching

1.2.2. Surface Micromachining

The surface micromachining relies on the thin film deposition above the substrate which is used as foundation for the mechanical structures. Two types of layer are used for structure development. These are the structural and sacrificial layers. The structural layers are formed the actual mechanical parts. They are commonly made by polysilicon. The main purpose of the using sacrificial layer is generating of suspended structures. The most common material is Silicon dioxide (SiO_2) for sacrificial layer [1].

In surface micromachining, the thin films are deposited and patterned by dry etching. At the end of the microfabrication, the sacrificial layers are etched by chemical solvents to obtain a suspended structure. The example of surface micromachining is shown in Figure 1.3.
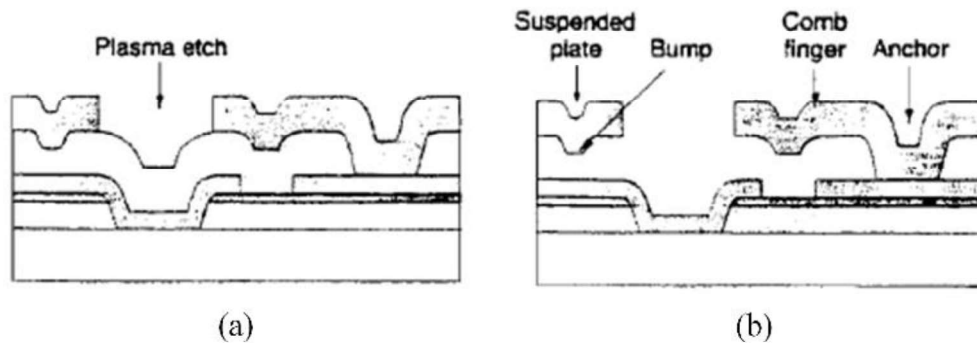
Figure 1.3. Formed structure with surface micromachining technique (a) before releasing, (b) after releasing [4]

In this example, the substrate is passivated and isolated with Silicon nitride (Si_3N_4) and SiO_2. Over the isolation layers, the sacrificial phosphosilicate glass (PSG) layer is deposited and patterned. Also, the dimples are formed by etching at that step. They are used as mechanical standoffs. After the sacrificial layers, the mechanical polysilicon layers are deposited by Low pressure chemical vapor deposition (LPCVD) at 610 °C. In order to doped polysilicon layer, the thin PSG layer is deposited and annealed at 1050 °C in N_2. Furthermore, the PSG layer is used to avoid stress gradient

in the structural layers. By using RIE, the mechanical structures are etched. After patterning them, the device is immersed into hydrofluoric acid (HF) to remove sacrificial layers [4].

The multiple structural and sacrificial layers are deposited to get desired device. However, each layer increases the complexity of the system. The statistical variations on the mechanical properties of the layers change the structure behavior. Furthermore, the stress is induced on the structural layers due to the fabrication processes that are performed on high temperature. All these problems bring along the adverse effects to the system behavior.

Especially, the residual stress significantly affects the suspended devices. The mechanical stiffness is changed, and their resonance frequencies shift. They may be buckled due to high residual stress on the device [5]. Thus, including residual stress effects increases the success rate of the device design.

1.3. Residual Stress on Thin Films

The residual stress on the thin films is originated from intrinsic and thermal stress. The intrinsic stress arises from the strain misfits which occur due to the phase transformation of the deposited layer. The thermal stress is generated by the thermomechanical properties mismatch of the layers. The total residual stress is summation of intrinsic and thermal stress [6].

High temperature variations are observed during the fabrication processes. Thus, thermal and mechanical properties of the materials become important criteria on the device performance. The fabrication layers are enlarged under this elevated temperature conditions depending on their coefficients of thermal expansion (CTE). When the two bonded layers expand unequally, they tend to bend [7].

As the multilayer structures are deposited over a substrate as shown in Figure 1.4, each layer is induced with stress. If the substrate is assumed as very thick and stiff, the stress on i^{th} layer can be calculated as in Equation 1.1 [8].

$$\sigma_i^R = -\frac{E_i(\alpha_i - \alpha_s)}{1 - \nu_i}\left(T - T_0^i\right) + \sigma_i^I \qquad (1.1)$$

where E_i, α_i, ν_i, σ_i^I, T_0^i are Young's Modulus, CTE, Poisson's ratio, intrinsic stress, deposition temperature of the thin film, respectively. α_s is the CTE of the substrate. Equation 1.1 gives the stress on each layer at any temperature T.
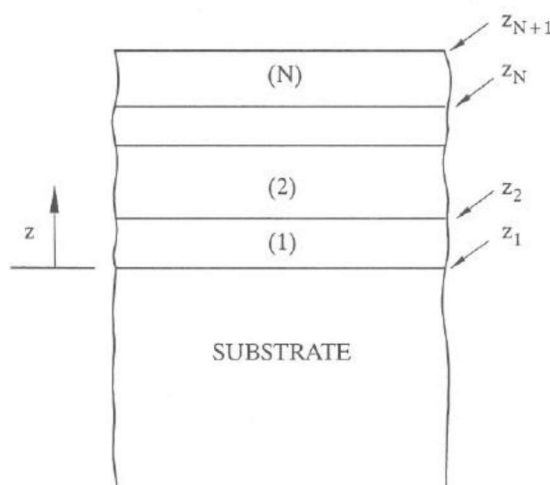
Figure 1.4. Multilayer deposition on a very thick substrate [8]

When the sacrificial etch is performed, the non-zero mean stress is detected on the film. Therefore, the out-plane film deformation happens due to non-uniform stress distribution over the film [6].

1.4. Effects of the Residual Stress on Suspended Membranes

The residual stress is a critical point that changes the characteristic of MEMS devices such as resonators, microphones, ultrasonic transducers. The performance of these devices is based on the sensitivity, natural frequency and the quality factor. However, the presence of the residual stress highly affects these parameters [9].

The induced stress determines the stiffness of the layer depending on the stress type. The compressive stress decreases the stiffness while the tensile stress increases. The stiffness alteration determines the dynamic characteristics of the device [10].

Especially, the compressive stress may buckle the device and block the proper operation. This buckling occurs if the device experiences with the compressive stress above the critical buckling stress. The larger or thinner membranes suffer from the residual stress since they have small critical stress value [11].

The membranes are designed to use as transmitter/receiver that operate a certain frequency range. The resonance frequency of the device restricts the operation range [12]. Like the stiffness, the resonance behavior of the suspended membranes is significantly affected by the induced stress since the resonance frequency is proportional to the ratio of residual stress and critical buckling stress value. Thus, the fundamental resonance frequency is mostly dominated by residual stress for the structure has a small critical buckling stress value. The resonance frequency decreases under compressive stress as it increases with tensile stress [13].

The resonance frequency may be controlled by the mechanical properties and dimensions of the membrane as interested with higher frequencies. In that region, residual stress effects can be ignored since stress domination on resonance frequency is diminished due to the higher critical buckling stress. However, residual stress should be included in resonance frequency calculation while working with the lower frequencies [14]. In that case, stress reduction improves the device performance by managing residual stress on the membrane.

1.5. Stress Reduction Methods

1.5.1. Metal Coating

Metal coating is usually performed by depositing gold layer which has a tensile stress on it. In this method, the gold layer is used to suppress the compressive stress of the membrane. The effective residual stress value depends on the ratio of the membrane layer thicknesses and individual stress values. Due to the tensile stress, it increases the stiffness and effective mass of the structure [9,15].

Because of the coating, it can be considered as bonded composite structure shown in Figure 1.5. Thus, the mechanical properties are calculated by adding effect of the gold layer.

Figure 1.5. Bonded composite structure

The effective flexural rigidity of a composite structure can be computed as [16]:

$$\frac{E_e t_e^3}{12} = \frac{E_1 t_1^3}{12} + E_1 t_1 \left(n - \frac{t_1}{2}\right)^2 + \frac{E_2 t_2^3}{12} + E_2 t_2 \left(t_1 - n - \frac{t_2}{2}\right)^2 \qquad (1.2)$$

where

$$K = \frac{E_2}{E_1} \qquad (1.3)$$

$$n = \frac{\frac{t_1^2}{2} + K t_2 \left(t_1 + \frac{t_2}{2}\right)}{t_1 + K t_2} \qquad (1.4)$$

E is the Young's Modulus of the layers and t is the thickness.

The effective residual stress for the multilayer structure can be calculated as [15]:

$$\sigma_{eff} = \frac{\sigma_1 t_1 + \sigma_2 t_2}{t_1 + t_2} \qquad (1.5)$$

In consequence of variation in effective residual stress and mechanical properties, the resonance frequency is shifted.

1.5.2. Corrugation

In corrugation method, the sacrificial layer is etched to obtain narrow trenches. Then, the structural layer is deposited over the sacrificial layer. The corrugated

membrane is achieved by performing sacrificial etch. The corrugation reduces the tension and mechanical stiffness of the membrane [17]. On the other hand, non-uniform thermal stress is observed in the membrane. Therefore, the thermal stress influence becomes more complicated than the flat membrane.

The corrugation profile factor (q) is the key parameter of the corrugated membrane shown in Figure 1.6. The trench depth (H) is used in the determination of the corrugation profile factor (q).
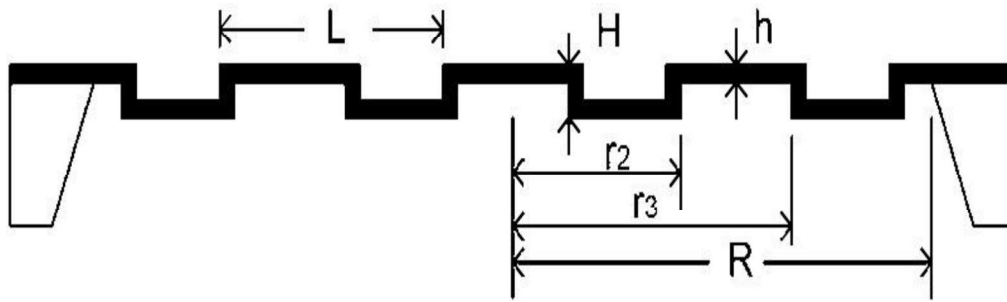
Figure 1.6. Cross sectional view of the corrugated membrane [18]

$$q^2 = 1 + 1.5 \frac{H^2}{h^2} \qquad (1.6)$$

For a corrugated membrane, the thermal stress is not uniform in the radial direction. The maximum stress is observed at the membrane edges. The radial thermal stress can be calculated as [18]:

$$\sigma(r) = -\frac{\Delta\alpha\, E\, \Delta T}{q} \left(\frac{r}{R}\right)^{q-1} \qquad (1.7)$$

Besides the membrane dimensions, the profile factor considerably affects the critical buckling stress value. Furthermore, it specifies the stress relaxation ratio of the structure that is the crucial effect on the resonance behavior. By accounting these alterations on mechanical properties of the system, the resonance frequency can be controlled [18].

1.6. Motivation of the Thesis

MEMS membranes are used as both transmitter and receiver in acoustic and ultrasound applications. Through the micromachining technologies, the membranes are fabricated with a wide range of size and shapes [12]. Mechanical behaviors of the membranes depend on the geometrical parameters, material properties and stress states. Their mechanical characteristics determine the operational frequency region. In addition, residual stress may buckle the device and prevent proper operation if it experiences a compressive stress above the critical buckling stress value.

Furthermore, MEMS membranes are electrostatically actuated in RF MEMS switches. Their actuation voltages depend on their mechanical properties and stress states [19]. Although the low actuation voltage is desired, unexpected switching might be observed. Tensile stress can be used to increase actuation voltage. However, it may cause the fractures by growth of cracks [18]. On the other hand, reasonably low actuation voltage improves CMOS compatibility of the device owing to low biasing voltage. Although the compressive stress reduces the actuation voltage, it affects device performance due to buckling [19].

Residual stress significantly affects the mechanical behavior of the membranes. Although relatively low stress values help us to design the devices with desired specifications, high stress values cause operational failures of the membrane. Stress relaxation techniques may improve the device performance by reducing the effects of the residual stress. Therefore, perforated membranes are proposed to manage the residual stress.

1.7. Objectives of the Thesis

In this thesis, perforation on the membrane is used to reduce the unfavorable effects of the residual stress. The holes ensure a remarkable stress relaxation on the membrane getting the buckling under control. The buckling-resistant (robust) membranes are designed with the help of perforation. They can properly operate under relatively high residual stress values compared to the critical buckling stress values.

Furthermore, the perforation changes the mechanical behavior of the device. The modified mechanical parameters are briefly derived for the membranes.

The critical buckling stress values and stress relaxation ratios are acquired from finite element method. The resonance frequencies are extracted via linear perturbation harmonic analysis. Furthermore, effects of the perforation ratio and hole radius are analyzed. The electrical characteristics of the membranes are investigated by electromagnetic simulations.

Owing to the reliable microfabrication, the proposed designs are fabricated. The electrical and optical characterization of the fabricated circular MEMS membranes are performed to investigate the advantages of the perforation. With the optical measurements, the resonance frequencies and vibrational modes are obtained. The FEM results are in harmony with the analytical solutions and experimental work. The stress management with the perforation is succeeded and verified by the experimental work and simulations.

CHAPTER 2

DESIGN AND FABRICATION OF THE MEMBRANE

2.1. Determination of Fabrication Process

As it was discussed before, the mechanical properties of the materials used in the fabrication is crucial to achieve proper operation. They significantly affect the membrane performance by causing the resonance frequency shift. Even they may be buckled due to residual stress after the sacrificial release is carried out. Thus, the process to be selected should have consistence and reliable fabrication data related to materials.

Under these concerns, the commercially available processes are investigated to find the process that has the most reliable and stable process flow. In addition to those features, the compatibility of the microfabrication with the proposed design is important to obtain desired devices. Considering the commercially available multi-user multi-processes (MUMPs), PolyMUMPs (MEMSCAP Inc., France) is chosen for the reliable fabricated devices found in the literature with PolyMUMPs [20-24].

2.2. PolyMUMPs

2.2.1. Overview of PolyMUMPs

Due to supporting many different device compositions, PolyMUMPs differs from most of the multi-user services since the process flow and the layer thicknesses are not developed for a single device configuration. PolyMUMPs consists of three structural layer polysilicon layer, two sacrificial oxide layers, one isolation layer and one metal layer as shown in Figure 2.1 [25]. Through three polysilicon structural layers, the desired devices are fabricated with different configurations. The sacrificial oxide layers are used in fabrication of the suspended devices. The Silicon nitride

ensures the electrical isolation between the substrate and structure. The main purpose of the metal layer is the electrical connection. On the other hand, it can be used to reduce stress on the devices as stated in stress reduction methods.
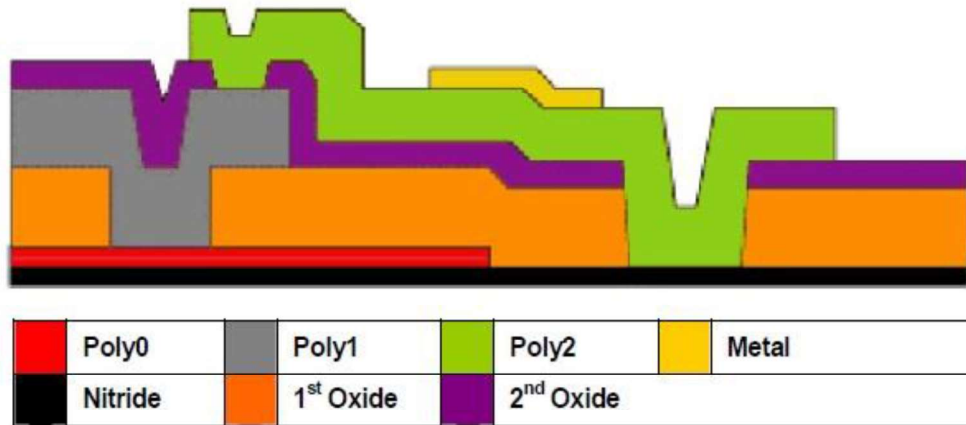
Figure 2.1. Cross sectional view of PolyMUMPs layers [25]

2.2.2. Process Flow of PolyMUMPs

The fabrication starts with the 150 mm n-type (100) silicon wafer [25]. 600 nm low stress LPCVD (Low pressure chemical vapor deposition) Silicon nitride layer is deposited over the wafer in order to provide electrical isolation between wafer and device. Then, the first structural polysilicon layer (Poly0) is deposited and patterned by photolithography. After patterning photoresist, Poly0 layer is etched in a plasma etch system.

The first sacrificial oxide layer (Oxide1, 2000 nm) is deposited by LPCVD and annealed 1050 °C for 1 hour. After the oxide deposition, reactive ion etched (RIE) is applied for DIMPLES mask to achieve small structural bumps which minimize the contact area between top and bottom electrodes. First oxide layer is also etched with ANCHOR1 mask to form anchor holes used in the electrical connections between Poly0 and the second structural polysilicon layer (Poly1).

This is followed by 2000 nm Poly1 deposition. It is lithographically patterned and etched. The second sacrificial oxide layer (Oxide2, 750 nm) is deposited after the

Poly1 is etched. Then, RIE is performed for POLY1_POLY2_VIA mask to etch the second oxide layer to reach Poly1. In addition, ANCHOR2 mask is used to etch both oxide layer in a single step to prevent misalignment. This mask provides electrical connection between Poly0 and the third structural layer (Poly2). Like Poly1, 1500 nm third structural layer (Poly2) is deposited and etched. The final deposition is 500 nm gold layer. It is patterned by using lift-off. The wafer is immersed into the 49% HF for 2 minutes to release the structure by removing oxide layers. Furthermore, supercritical CO_2 drying is performed after HF release in order to prevent device stiction [25].

2.2.3. Parameters of Thin Films used in PolyMUMPs

Thin film parameters are one of the critical parts for the membrane design since the resonance frequency of the proposed design is determined by these parameters. They are provided by MEMSCAP based on the previous runs which are performed since the early 1990's. Due to long-time experienced, the reliable data is shared with the designers. According to supplied data, the Young's Modulus of the structural polysilicon layer is 158 +/- 10 GPa and the Poisson's ratios is 0.22 +/- 0.01 [24]. Furthermore, typical thickness, residual stress and resistance values are listed in Table 2.1.

Table 2.1. *Nominal thin film parameters of PolyMUMPs process layers [25]*

Film	Thickness (nm)	Residual Stress (MPa)	Resistance (Ohm/sq)
Nitride	600	90	N/A
Poly0	500	-25	30
Oxide1	2000	N/A	N/A
Poly1	2000	-10	10
Oxide2	750	N/A	N/A
Poly2	1500	-10	20
Metal	520	50	0.06

2.3. Design of the Membrane

2.3.1. General Structure of the Membrane

There are three structural layers in PolyMUMPS to create own structure. However, only two of them can be suspended membrane layer since at least one layer should be used to support the membrane. In order to have the higher gap between membrane and bottom surface, Poly2 layer is chosen as suspended membrane layer since higher gap is reduced the stiction probability of the membrane. Thus, the general structure is designed as shown in Figure 2.2.
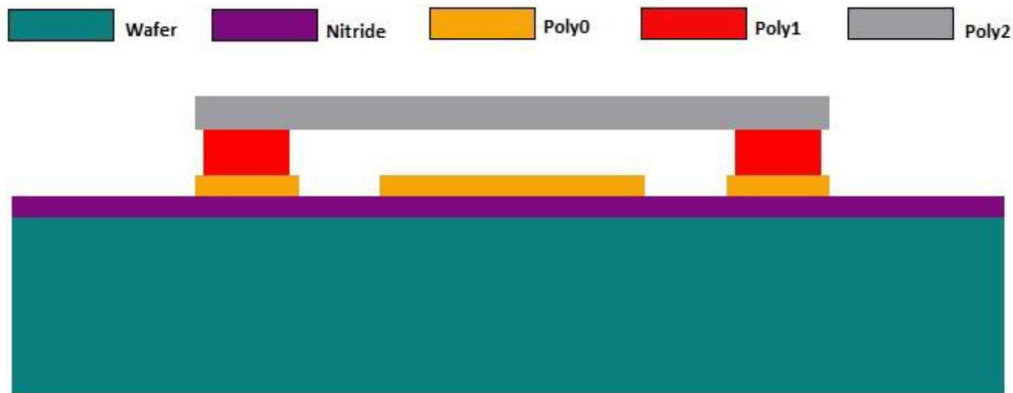
Figure 2.2. General structure of the proposed design

Poly0 layer has two main objectives which are acting as a bottom electrode and supporting the membrane. Poly0 layer placed to the center is used as ground electrode. The others support the membrane with Poly1 layer. Suspended membrane is formed from Poly2 layer which is fixed from the edges to the substrate. The nitride layer provides electrical isolation between the structure and substrate.

2.3.2. Determination of the Membrane Dimensions

2.3.2.1. Resonance Frequency of the Solid Circular Diaphragm

The membrane design is strongly dependent to resonance behavior of the system since the response of the membrane dramatically decreases above the resonance frequency. Thus, the resonance frequency estimation is crucial for a proper

14

operation. In a non-stressed clamped circular membrane, the resonance frequency is calculated by Equation 2.1 [26].

$$f_{m,n} = \frac{\lambda_{m,n}}{2\pi} \frac{t}{r^2} \sqrt{\frac{E}{12\rho(1-v^2)}}$$

(2.1)

The resonance frequency is proportional to mode coefficient ($\lambda_{m,n}$), thickness (t) and Young's modulus (E) of the membrane. It is inversely proportional with radius (r), mass density (ρ), Poisson's ratio (v). The first four mode coefficient are listed in Table 2.2.

Table 2.2. *Mode coefficient of the clamped circular membrane [26]*

Mode (m, n)	*Coefficient value*
0,1	10.22
1,1	21.26
2,1	34.88
0,2	39.77

The first four mode shapes of the circular membrane are shown in Figure 2.3 [27]

m = 0, n = 1   m = 1, n = 1

m = 2, n = 1   m = 0, n = 2
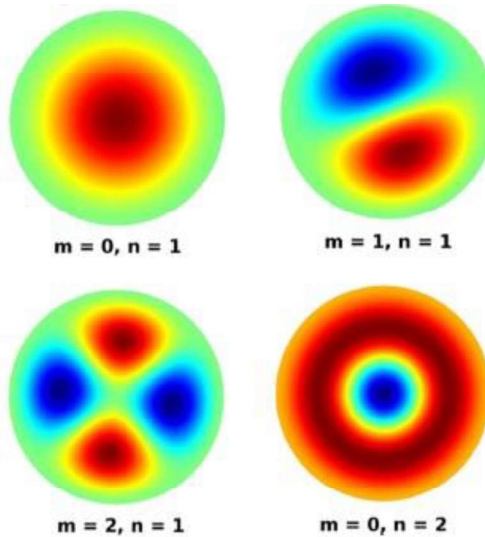
Figure 2.3. First four vibrational mode shapes of the circular membrane [27]

By using Equation 2.1, the resonance frequencies of the solid circular membrane are calculated for different radius values. Young's Modulus, Poisson's ratio, density and thickness are assumed as 158 GPa, 0.22, 2332 kg/m^3, 1.5 µm, respectively. The resonance frequencies are shown in Figure 2.4.
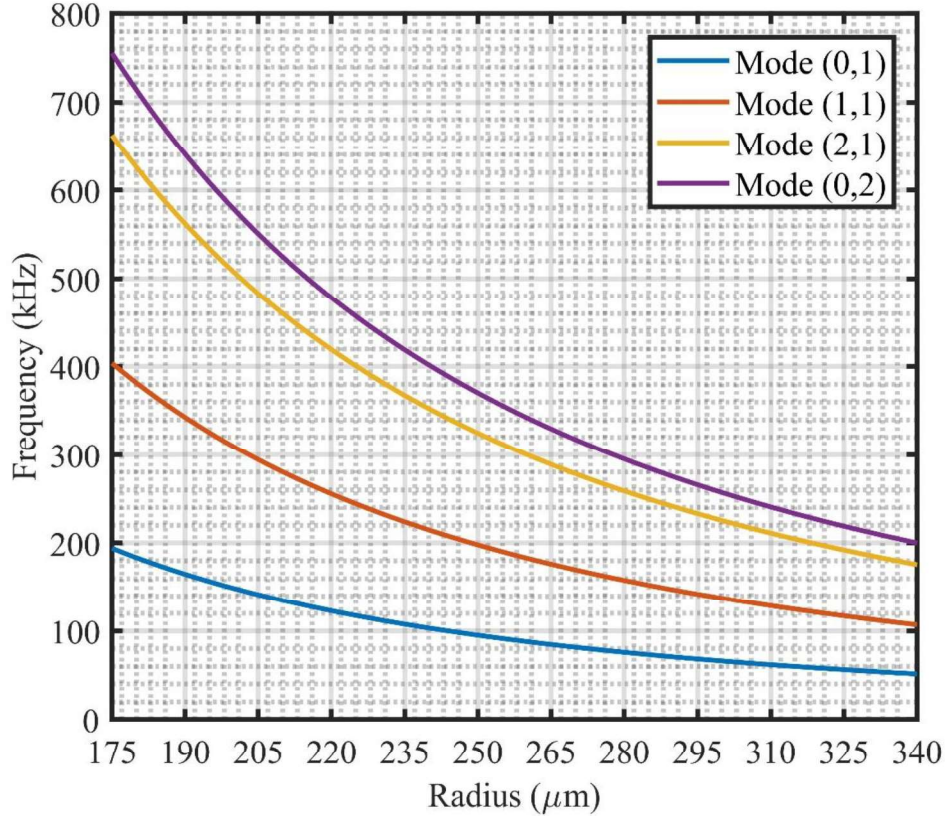
Figure 2.4. Resonance frequencies of solid circular membrane for different radius values

2.3.2.2. Residual Stress Effect on the Resonance Frequency

Residual stress on the membrane may cause a significant shift in the resonance frequency depending on the critical buckling stress value of the membrane. The relationship between the residual stress and resonance frequency is stated in Equation 2.2

$$f'_{m,n} = f_{m,n} \sqrt{1 + \frac{\sigma_{res}}{\beta_{m,n}\, \sigma_{cr}}} \tag{2.2}$$

where σ_{res} is the residual stress in the membrane, σ_{cr} is the critical buckling stress value, $\beta_{m,n}$ is the stress effect factor. For the higher vibration modes, the percentage of the resonance frequency shift decreases with increasing stress effect factor [14,28]. It can be assumed as in the Equation 2.3.

$$\beta_{m,n} \cong \frac{\lambda_{m,n}}{\lambda_{0,1}}$$

(2.3)

The critical buckling stress value formula is given in the Equation 2.4 for the clamped circular membrane in order to calculate the resonance frequency shift [29]. Also, the critical stress values are obtained for different radius values by using Equation 2.4. It is shown in Figure 2.5.

$$\sigma_{cr} = 14.68 \frac{E}{12\ (1 - v^2)} \left(\frac{t}{r}\right)^2$$

(2.4)
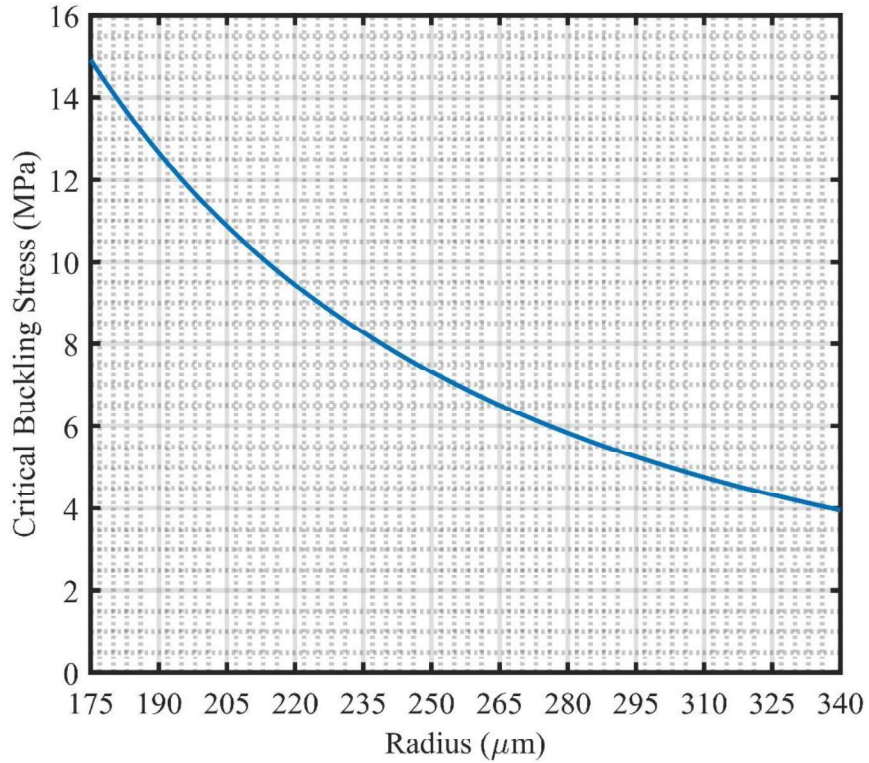
Figure 2.5. Critical buckling stress values of solid circular membrane for different radius values

For the proposed design, the membrane has -10 MPa residual stress as stated by MEMSCAP. It makes sense to choose the critical buckling stress value as close as the residual stress since the stress relaxation effectiveness can be seen easily with the applied method. Thus, 220 µm and 205 µm are chosen for the membrane radius. Their critical stress values are 9.44 MPa and 10.87 MPa, respectively.

For the selected radii, the first resonance frequencies are obtained by sweeping the residual stress values to interpret the residual stress effect. As shown in Figure 2.6, the resonance behavior vanishes if the membranes are experienced with the residual stress that is higher than the critical buckling stress values. In that region, Equation 2.2 has imaginary solution since the membrane has buckled. Furthermore, the resonance frequency dramatically shifts as the residual stress approaches the critical stress.
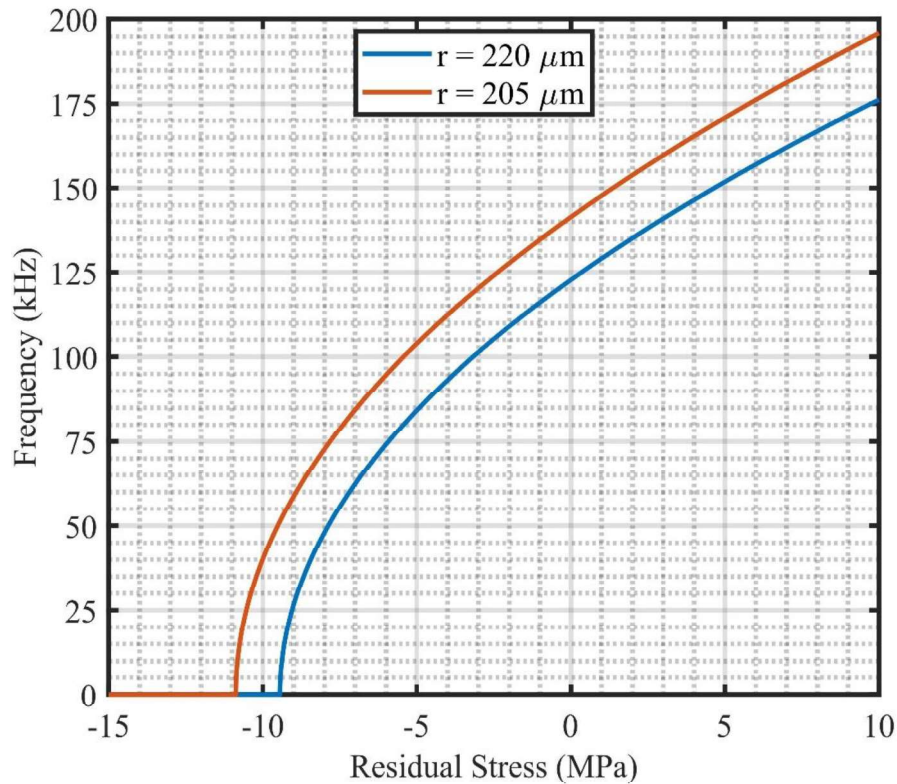
Figure 2.6. First resonance frequencies for the selected membranes under different residual stress values

18

2.3.2.3. Perforation Effect on the Resonance Frequency

By placing holes on the membrane, the mechanical properties of the membrane are changed depending on the ligament efficiency and perforation type [30]. The perforations patterns and ligament efficiency parameters are shown in Figure 2.7.
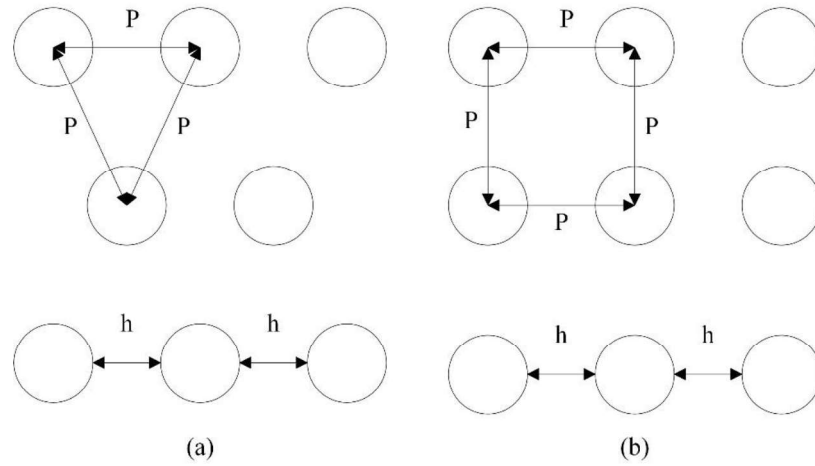
Figure 2.7. (a)Triangular, (b) Square pattern perforation

The ligament efficiency can be expressed as in Equation 2.5. Based on the ligament efficiency, the mass density, Poisson's ratio and Young's Modulus of the membrane are modified. The mechanical stiffness of the membrane decreases. Thus, the resonance frequency should be calculated with modified mechanical parameters [31].

$$\eta_l = \frac{h}{P} \tag{2.5}$$

Instead of estimating all mechanical properties for the perforated plates, it is possible to calculate resonance frequency by assuming that only Young's Modulus is changed, and the other parameters are the same. Regarding this assumption, effective Young's Modulus of triangular and square pattern perforation can be calculated as shown in Equation 2.6 and 2.7, respectively [30].

$$\frac{E_{tri}}{E} = 0.6106 + 1.1253\eta_l - 2.7118\eta_l^2 + 4.0812\eta_l^3 - 2.1128\eta_l^4 \qquad (2.6)$$

$$\frac{E_{squ}}{E} = 0.5280 + 2.0035\eta_l - 5.4758\eta_l^2 + 7.7474\eta_l^3 - 3.8968\eta_l^4 \qquad (2.7)$$

In order to understand the perforation effect, the first resonance frequencies are obtained with ligament efficiency sweep by ignoring the residual stress effect. Unity ligament efficiency means that no hole exists in membrane. On the other hand, zero ligament efficiency indicates that the plate is completely perforated. As shown in Figure 2.8, the perforation patterns differ in the extreme points where the ligament efficiency is close to 0 or 1. Apart from this, there is no distinct difference between the perforation types when the residual stress is ignored.
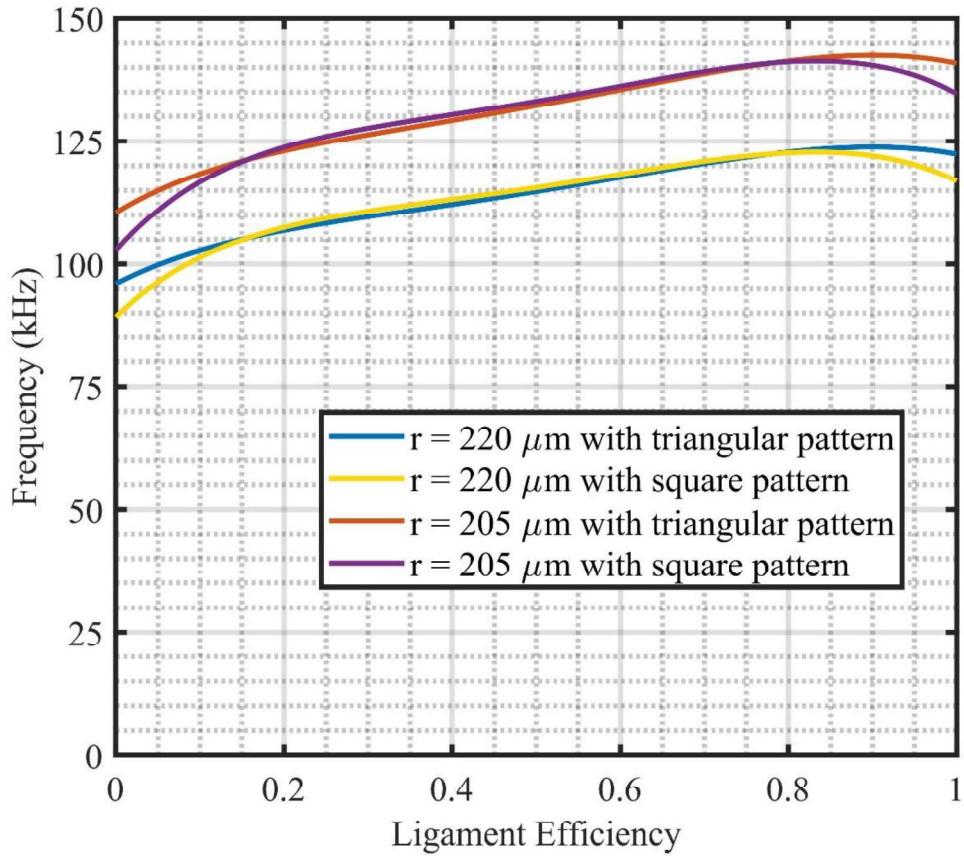
Figure 2.8. First resonance frequencies for the selected membranes with various ligament efficiencies and patterns

In the proposed design, the perforation ratio is crucial to prevent the buckling since it will be used to reduce stress on the membrane. From this point of view, the perforation type becomes important. Figure 2.9 is used to calculate fill factor (FF).
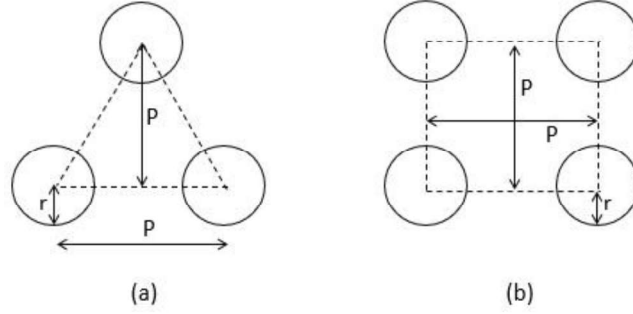
Figure 2.9. Dimensional representation of the perforation types

$$FF_{triangular} = \frac{\left(\frac{P^2}{2} - \frac{\pi r^2}{2}\right)}{\frac{P^2}{2}} = 1 - \frac{\pi r^2}{P^2} \tag{2.8}$$

$$FF_{square} = \frac{(P^2 - \pi r^2)}{P^2} = 1 - \frac{\pi r^2}{P^2} \tag{2.9}$$

The fill factors are also equal for the perforation types. Therefore, both perforation types can be used in the fabrication. However, the triangular perforation is more beneficial than the square one in the sacrificial releasing step since the holes are closer in diagonal direction. Thus, the triangular pattern is chosen. However, there is a small difference between applied triangular perforation pattern and found in literature due to discretization of the fabrication masks.

The last step is determination of the hole radius. The main concerns are buckling and sensitivity. The fill factor should be high enough to prevent buckling and achieve detectable signal level. As the fill factor decreases, the signal level also decreases. However, the stress relaxation increases [32,35]. The fill factor is aimed as 75% to find the optimum point. Therefore, hole radius is chosen as 8 μm and the distance of the two adjacent hole centers (P in Figure 2.9) is 28 μm. Based on these parameters, fill factor is obtained as 74.35% and the ligament efficiency is 3/7.

2.3.2.4. Proposed Design Parameters

Two membranes are chosen to be fabricated based on the perforation and residual stress effects. They have the same fill factors and hole radii. The only difference is the membrane radius. Therefore, they exhibit different buckling behavior. The chosen design parameters are listed in Table 2.3.

Table 2.3. *Parameters of the proposed design*

Design	Membrane Radius (μm)	Membrane Thickness (μm)	Hole Radius (μm)	Perforation Type	Ligament Efficiency
A	220	1.5	8	Triangular	3/7
B	205	1.5	8	Triangular	3/7

2.4. Preparation of the Fabrication Mask

Before starting the mask drawing, PolyMUMPs design rules are studied to prevent the fabrication failures. All mandatory and advisory rules are examined. The mask drawing is performed carefully not to violate the rules. The mask drawing is handled with Tanner L-Edit (Mentor Graphics Corporation, Wilsonville). Furthermore, the macro feature of L-Edit is used to achieve similar membranes with minor dimension changes. In the macro file, the dimensions are defined as parameters. By changing them, the proposed design masks are obtained.

Although there are twelve fabrication masks in PolyMUMPs, six of them are utilized in the proposed design. These masks are POLY0, ANCHOR1, POLY1, POLY1_VIA_POLY2, POLY2, HOLE2.

Firstly, POLY0 mask is created as shown in Figure 2.10 to indicate the ground electrode and signal path. The radius of the ground electrode at the center is 65 μm smaller than the membrane radius. Also, it is used to support the membrane from edges. 24º gap is found for Poly0 layers.
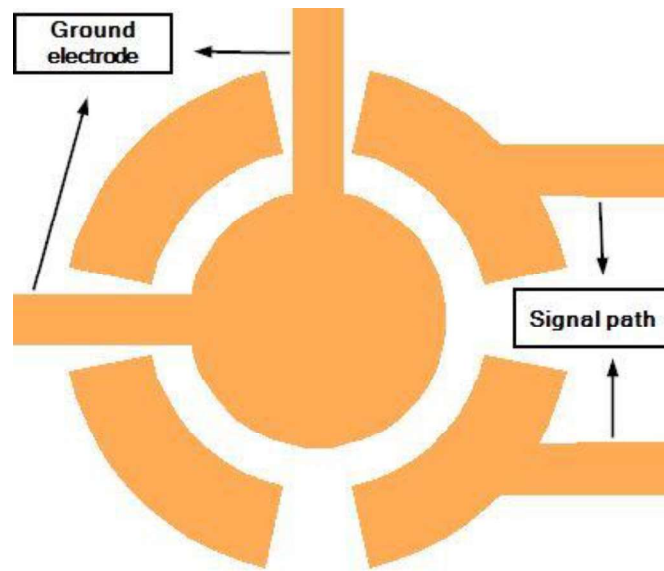
Figure 2.10. POLY0 fabrication mask

Over the POLY0, the ANCHOR1 mask is drawn as shown in Figure 2.11 to remove sacrificial oxide from the indicated regions with ANCHOR. In this way, the electrical connection will be provided between Poly1 and Poly0 layer.
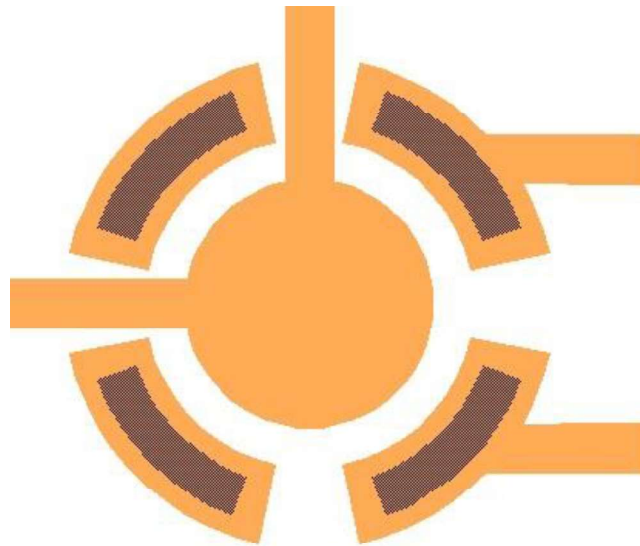
Figure 2.11. POLY0 (orange) and ANCHOR1 (gray) masks

23

POLY1 mask is utilized to fill the removed oxide regions with Poly1 layer which is used as second supporting layer. It is shown in Figure 2.12.
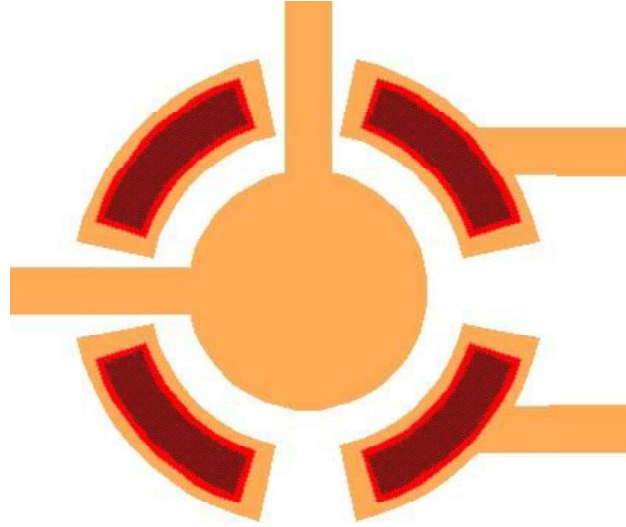
Figure 2.12. POLY0 (orange), ANCHOR1 (gray) and POLY1 (red) masks

POLY1_VIA_POLY2 mask is used to electrically connect the Poly2 and Poly1 layers by removing oxide layer where it is drawn. It can be seen in Figure 2.13.
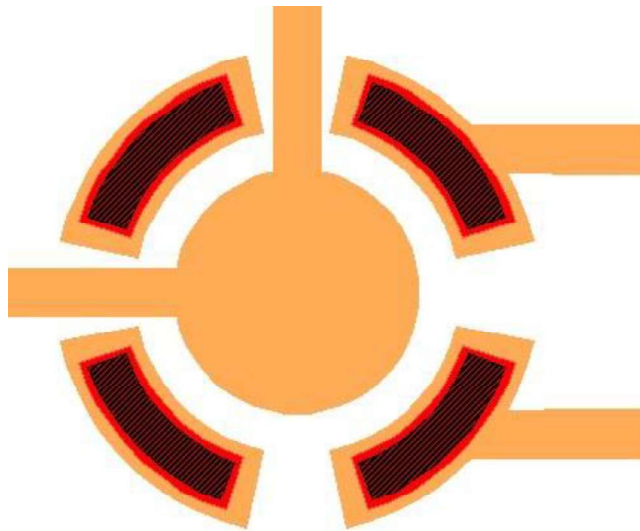
Figure 2.13. POLY0 (orange), POLY1 (red) and POLY1_VIA_POLY2 (black) masks

For the last step, POLY2 and HOLE2 mask are drawn as in Figure 2.14 to form the suspended membrane with holes. The same procedure is applied for Design B as well in Figure 2.15.
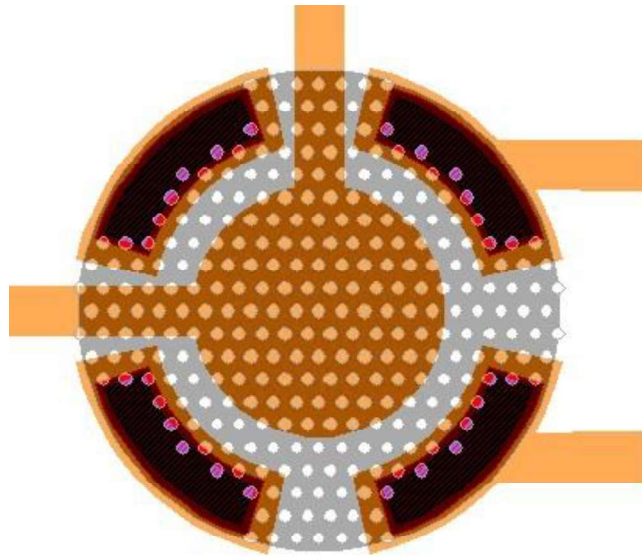
Figure 2.14. Final mask of Design A
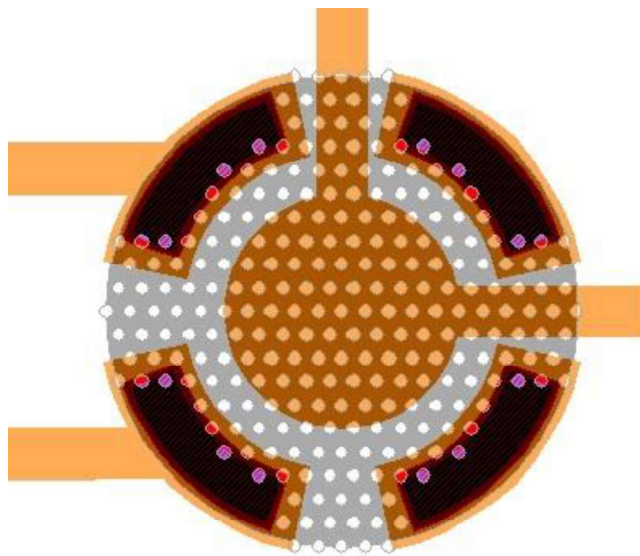
Figure 2.15. Final mask of Design B

2.5. Microfabrication Modelling

Although the design masks are drawn in Tanner L-Edit (Mentor Graphics Corporation, Wilsonville), the microfabrication is simulated in SEMulator3D 8.0 (Coventor, North Carolina) before the membranes are fabricated. It is a powerful tool for semiconductor and MEMS process modelling. It has advanced etching and deposition process steps used in PolyMUMPS such as LPCVD, RIE, lift-off. Furthermore, it provides 3-D structure profiles after each process step. By this means, it is used to detect any possible failures on microfabrication due to misinterpreted process step.

PolyMUMPs process flow is defined in SEMulator3D as provided by MEMSCAP. The same etch and deposition processes are used with the correct layer parameters. The mask drawn in Tanner L-Edit is imported into SEMulator3D. Then, the 3D models and cross-sectional views are obtained for the proposed designs.

The design details are clearly seen from the cross-sectional and isometric view. Poly0 and Poly1 layers support the membrane from edges. Electrical isolation is provided by Nitride layer. The ground electrode is formed by Poly0 at the center. Furthermore, the symmetrical hole distribution can be seen from isometric view.
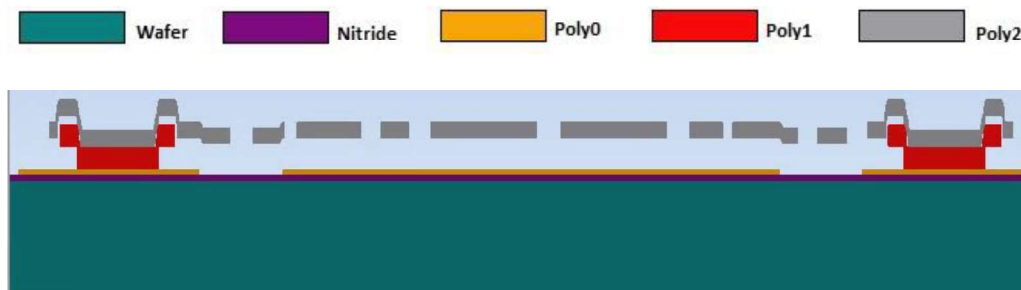
Figure 2.16. Cross sectional view of Design A
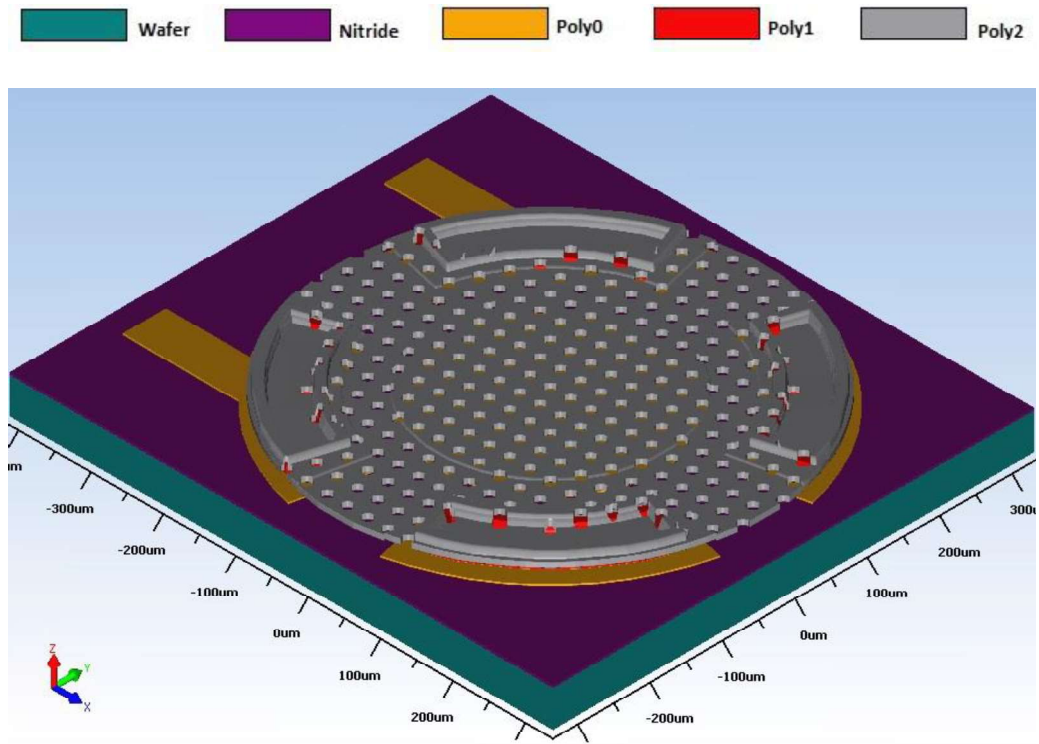
Figure 2.17. Isometric view of Design A

In addition, the two extended signal paths formed by Poly0 layer are shown. They are connected to the electrical pads to receive vibrational signals from the membrane. The equally separated holes are inspected in Figure 2.18 by taking cross-sectional view at the center of the membrane.
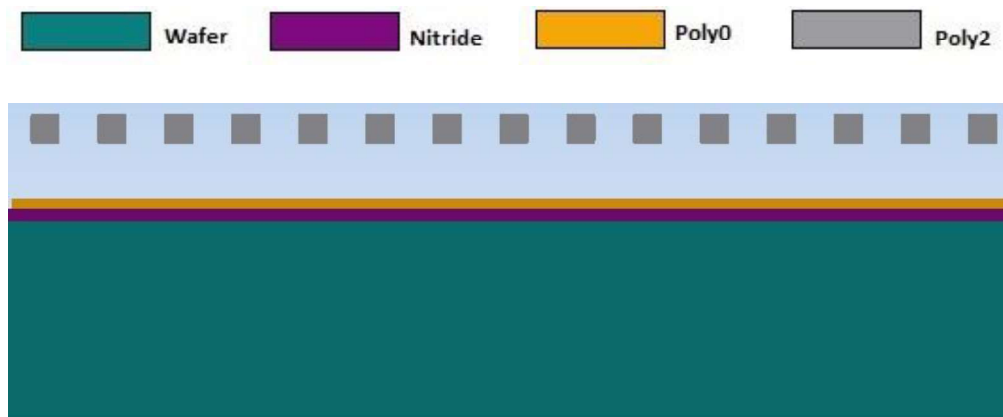
Figure 2.18. Hole distribution on the proposed designs

The same procedure is applied for the Design B, and the 3D models are acquired as shown in Figure 2.19 and Figure 2.20. They are identical with Design A except the membrane radius as well as the hole counts.
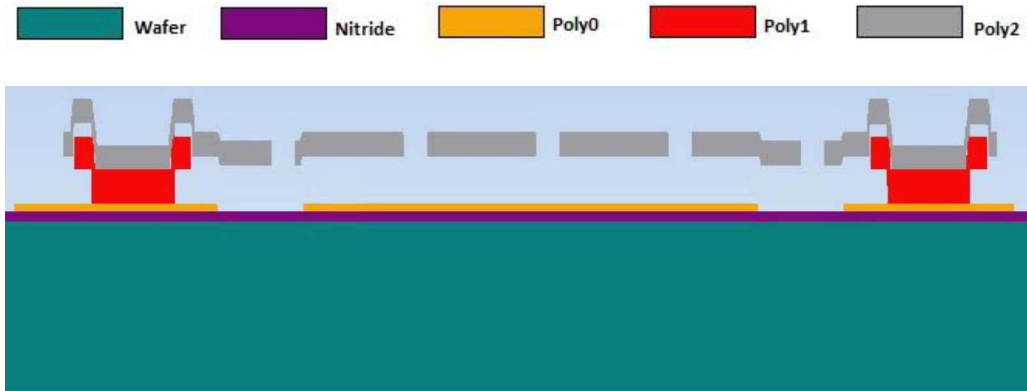
Figure 2.19. Cross sectional view of Design B
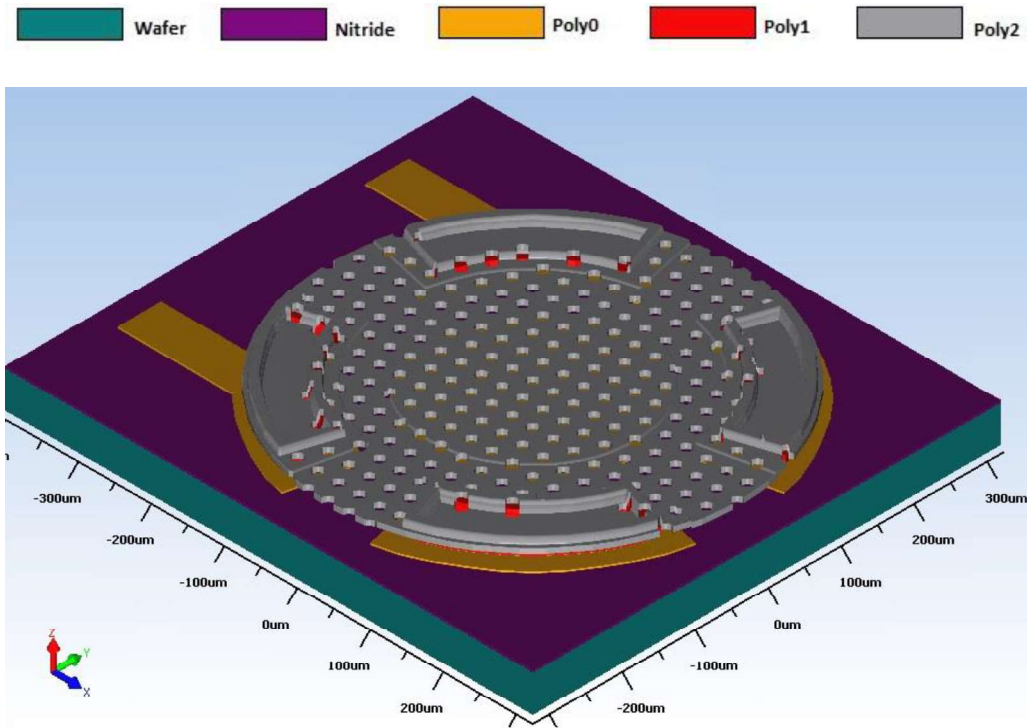
Figure 2.20. Isometric view of Design B

Output of the microfabrication modelling ensures that there is no design failure in the mask drawing. All masks are used in the correct way to obtain desired device. The suspended membrane is formed as described before. The support layers (Poly1 and Poly0) are placed as it is supposed to be. The ground and signal paths are created properly. Most importantly, it shows that the PolyMUMPs process flow is well understood. There is no doubt about the microfabrication. The fabrication masks are confidently submitted to the MEMSCAP.

CHAPTER 3

FINITE ELEMENT ANALYSIS

3.1. Mechanical Simulations

Mechanical simulations of the proposed membranes are carried out by using a commercially available finite element analysis package (ANSYS 19.2, Ansys Inc., Canonsburg, USA). The 3D structure of the membrane is formed with Ansys Parametric Design Language (APDL). Although mesh export is possible from SEMulator3D, APDL is used to provide flexibility in case of minor changes related to dimensions. By this way, proposed membranes are constituted with changing key parameters such as hole placement, membrane radius, hole dimensions, hole separation and support type. Thus, any error originating from ANSYS model is prevented.

3.1.1. Formation of the Geometrical Models in ANSYS

Based on the fabrication masks, the membranes are created step by step. First of all, the bare substrate is generated, and it is covered by nitride. Over these layers, the support layers and bottom electrode are constituted as shown in Figure 3.1. The gap between the support layers is identical with the fabrication mask. It is 24º for Poly0 layers, and 36º for Poly1 layers.

As the last step, the suspended membrane is placed over the Poly1 layer. Also, the small circular holes are removed from the Poly2 layer as shown in Figure 3.1 (a). In order to provide interaction between the layers, they have glued with each other. With the same ANSYS code, Design B is also generated by changing the membrane radius and hole counts as shown in Figure 3.1 (b)

Wafer   Nitride   Poly0   Poly1   Poly2
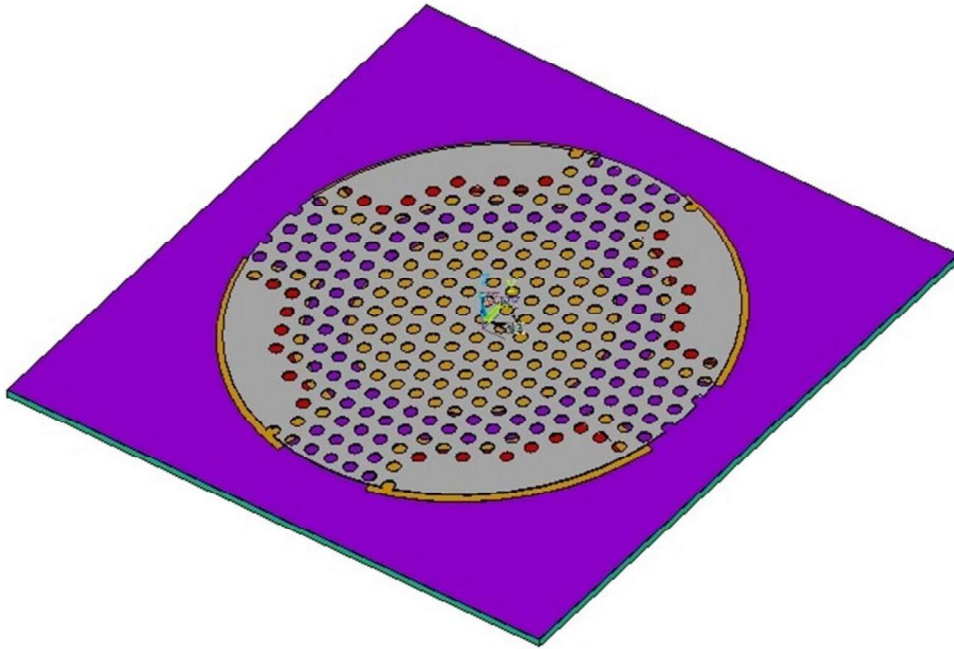
(a)
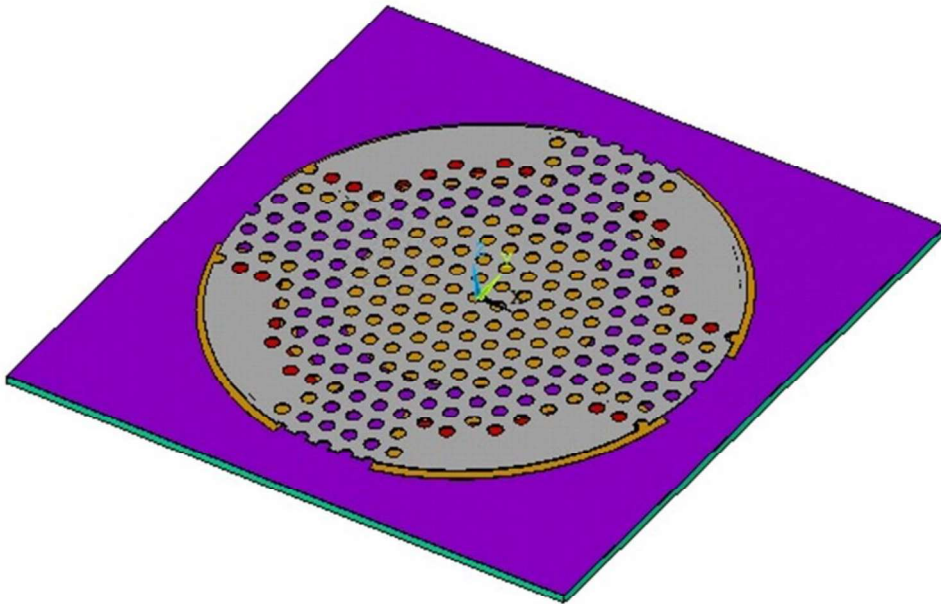
(b)

Figure 3.1. Isometric view of (a) Design A, (b) Design B in ANSYS

3.1.2. Properties of Element and Materials used in ANSYS

The higher order 3-D 20-node solid element (SOLID186) is chosen to perform the static and harmonic analyses. It exhibits quadratic displacement behavior. Furthermore, it has stress-stiffening, large deflection, and large strain capabilities which are critical for the non-linear behaviors [33].

The mechanical properties are set as shown in Table 3.1. Only Young's Modulus, Poisson's ratio and density are required for the mechanical simulations. The membrane thickness is the same with the Poly2 layer thickness which is stated as 1.5 µm by MEMSCAP.

Table 3.1. *Mechanical properties of the materials used in simulation*

Material	Young's Modulus (GPa)	Poisson's Ratio	Density (kg/m³)
Polysilicon	158	0.220	2332
Nitride	320	0.263	3270

3.1.3. ANYS Model Configurations

To compare the FEM results with both analytical solutions and experimental results, the different configurations are composed. For this purpose, hole radius and support types are changed in ANSYS models. The hole radius is chosen as 4, 6, 8 µm. Moreover, the solid membranes which has no hole are created.

In fabricated membranes, support is divided into four symmetric parts. However, the support with a single part is also constructed in ANSYS to hold the membrane from all edge points. The created ANSYS models are listed with their key parameters in Table 3.2.

Table 3.2. *Composed ANYS Models with key parameters*

Model Number	Membrane Radius (μm)	Hole Radius (μm)	Ligament Efficiency	Support Type
1	220	-	-	Single part
2	220	4	5/7	Single part
3	220	6	4/7	Single part
4	220	8	3/7	Single part
5	220	8	3/7	Four parts
6	205	-	-	Single part
7	205	4	5/7	Single part
8	205	6	4/7	Single part
9	205	8	3/7	Single part
10	205	8	3/7	Four parts

While changing the hole radius, the distance between two adjacent hole centers is kept as 28 μm. Thus, the holes are placed on the same locations with the other ones. By this way, the effect of the hole radius can be easily observed. Furthermore, the support types are shown in Figure 3.2 to avoid the confusion.
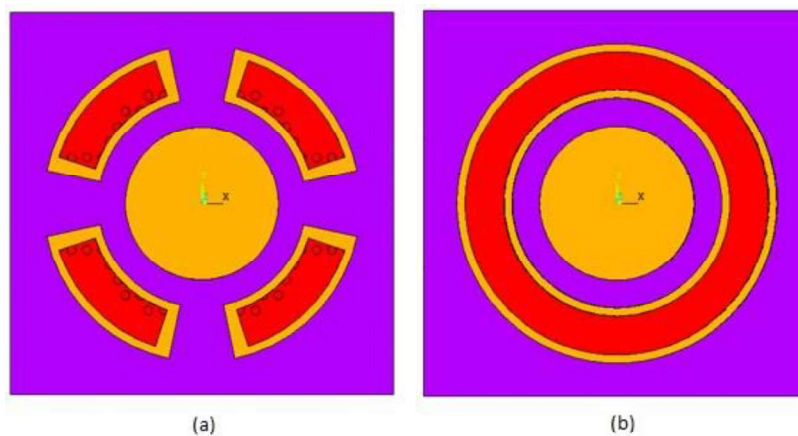
Figure 3.2. (a) Four parts, (b) single part support in ANSYS

3.1.4. ANSYS Analyses

The FEM is used to extract critical stress values and resonance frequencies based on the displacement of the prestressed membrane. Boundary conditions are applied to be solved differential equations properly. For this purpose, the bottom of the substrate is fixed from all directions (x, y, z) in analyses.

3.1.4.1. Static Analysis Results and Discussions

The critical stress values are found for the membranes by using static analysis. The Poly2 layer is initially induced with stress by INISTATE command. Furthermore, non-linear effects such as large deflection and stress-stiffening are included with NLGEOM command. It is crucial for the thin structures in which bending stiffness is very small compared to axial stiffness [34].

Static analysis is performed by sweeping stress values to find the critical point which is the displacement behavior changing due to buckling. Thus, the applied initial stress is swept from 15 MPa to -15 MPa with 0.1 MPa steps. Also, the volume based average stress is calculated for the Poly2 layer in order to determine the stress relaxation ratio. The static analysis results are shown in Table 3.3.

Table 3.3. *Stress relaxation and critical buckling stress values found in static analysis*

Model Number	*Average Stress Relaxation (%)*	*Applied Stress on Buckling (MPa)*	*Critical Buckling Stress (MPa)*
1	1.76	-9.8	-9.53
2	8.75	-9.8	-8.94
3	16.67	-10.4	-8.67
4	25.75	-11.6	-8.61
5	33.39	-12.4	-8.25
6	1.87	-11.1	-10.89
7	8.75	-11.3	-10.30
8	16.67	-11.9	-9.88
9	25.79	-13.2	-9.78
10	33.39	-14.1	-9.36

The critical buckling stress values of Model 1 and 6 can be calculated by using Equation 2.4 since they are solid membranes with a radius 220 µm and 205 µm. The critical buckling values are found as -9.44 MPa and -10.87 MPa. The deviations of the ANSYS simulation results are 0.95% and 0.18%.

The induced average stress on the membrane is divided by the initially applied stress to find the stress relaxation. By calculating stress relaxation for 301 stress values changing from -15 MPa to 15 MPa, average stress relaxation percentages are acquired as in Table 3.3.

Table 3.3 implies that the support type and hole size significantly affect the stress relaxation and buckling. The stress relaxation increases with decreasing fill factor. In other words, the smaller holes cause larger mechanical stiffness and less stress relaxation. Furthermore, the stress relaxation increases when the membrane is not supported from all edge points. The spacing on the supports helps the membrane to be relaxed.

Also, the ligament efficiency is effective on the stress relaxation. Although the membrane radius is changed, the stress relaxation remains the same due to the identical ligament efficiencies. The stress relaxation directly affects the durability of the membranes against the residual stress. Although the larger holes reduce the mechanical stiffness and critical buckling stress value, less stress is induced on the membranes. Thus, they can operate under higher stress values without buckling.

3.1.4.2. Harmonic Analysis Results and Discussions

The resonance frequencies are found with the linear perturbation full-harmonic analysis. This procedure consists of the two consecutive analyses which are the static and full-harmonic analysis [33].

Firstly, the static analysis is conducted with the same procedure applied on critical stress value determination with an exception. It is performed for the pre-determined stress value instead of stress sweeping. The computed stiffness matrix is

used as an input for the full harmonic analysis. In this way, the prestress influences on the structure stiffness is included.

For the full harmonic analysis, uniform pressure is applied top of the membrane for the excitation purpose. The membrane displacement is saved for distinct frequencies. Then, the resonance frequencies are detected by investigating the displacement on radial positions.

The linear perturbation harmonic analysis is performed to extract resonance frequencies under residual stress. The applied initial stress is swept from -15 MPa to 10 MPa with 1 MPa steps. For each stress value, the harmonic analysis is carried out with a frequency sweep from 1 kHz to 650 kHz with 1 kHz steps.

In order to calculate the theoretical resonance frequencies, output of the static analysis is also included since critical buckling stress value and induced stress on the membrane are required. Model dimensions, material properties and the static analysis results are inserted into Equation 2.1 and 2.2 to obtain the resonance frequencies.

During the harmonic analysis, the main objective is investigation of the perforation effects on the resonance frequency. Thus, ten different ANYS models are used in harmonic analysis. The hole radius and membrane radius are changed to find the dimension related effects. Also, the support type is changed to obtain the same structure with fabricated devices. They are used for the comparison of the experimental data.

The presence of the hole is analyzed by simulating the Model 1 and Model 4. Their membrane radii are 220 μm. However, Model 1 has no hole while hole radius of Model 4 is 8μm. These models are simulated with linear perturbation harmonic analysis method. Their results are listed in Table 3.4 and Table 3.5.

Table 3.4. *Harmonic analysis results for Model 1 (membrane radius = 220 μm, without hole, support= single part)*

Applied Stress (MPa)	Induced Stress (MPa)	Theoretical f(0,1) (kHz)	Simulated f(0,1) (kHz)	Error f(0,1) (%)	Theoretical f(0,2) (kHz)	Simulated f(0,2) (kHz)	Error f(0,2) (%)
-15	-14.74	NA	NA	**NA**	370.94	353	**4.84**
-14	-13.75	NA	NA	**NA**	379.00	364	**3.96**
-13	-12.77	NA	NA	**NA**	386.90	374	**3.33**
-12	-11.79	NA	NA	**NA**	394.64	384	**2.70**
-11	-10.81	NA	NA	**NA**	402.23	394	**2.05**
-10	-9.82	NA	NA	**NA**	409.68	403	**1.63**
-9	-8.84	30.98	33	**6.53**	416.99	413	**0.96**
-8	-7.86	50.28	52	**3.42**	424.18	422	**0.51**
-7	-6.88	64.01	66	**3.11**	431.25	431	**0.06**
-6	-5.89	75.27	78	**3.63**	438.21	439	**0.18**
-5	-4.91	85.05	87	**2.29**	445.06	448	**0.66**
-4	-3.93	93.82	96	**2.32**	451.80	456	**0.93**
-3	-2.95	101.84	104	**2.12**	458.44	465	**1.43**
-2	-1.96	109.27	112	**2.50**	464.99	473	**1.72**
-1	-0.98	116.23	118	**1.53**	471.45	481	**2.03**
0	0.00	122.79	125	**1.80**	477.82	488	**2.13**
1	0.98	128.96	131	**1.58**	484.11	496	**2.46**
2	1.96	134.85	137	**1.59**	490.32	504	**2.79**
3	2.95	140.50	142	**1.07**	496.45	511	**2.93**
4	3.93	145.93	148	**1.42**	502.50	518	**3.08**
5	4.91	151.16	153	**1.22**	508.48	526	**3.44**
6	5.89	156.21	158	**1.14**	514.40	533	**3.62**
7	6.88	161.11	163	**1.17**	520.24	540	**3.80**
8	7.86	165.87	167	**0.68**	526.02	547	**3.99**
9	8.84	170.49	172	**0.89**	531.74	554	**4.19**
10	9.82	174.98	176	**0.58**	537.40	561	**4.39**

Table 3.5. *Harmonic analysis results for Model 4 (membrane radius = 220 µm, hole radius = 8 µm, support = single part)*

Applied Stress (MPa)	Induced Stress (MPa)	Theoretical f(0,1) (kHz)	Simulated f(0,1) (kHz)	Error f(0,1) (%)	Theoretical f(0,2) (kHz)	Simulated f(0,2) (kHz)	Error f(0,2) (%)
-15	-11.14	NA	NA	**NA**	358.83	350	**2.46**
-14	-10.39	NA	NA	**NA**	364.74	358	**1.85**
-13	-9.65	NA	NA	**NA**	370.55	365	**1.50**
-12	-8.91	NA	NA	**NA**	376.28	373	**0.87**
-11	-8.17	25.60	22	**14.05**	381.92	380	**0.50**
-10	-7.43	41.87	41	**2.07**	387.47	387	**0.12**
-9	-6.68	53.40	54	**1.13**	392.95	395	**0.52**
-8	-5.94	62.85	64	**1.83**	398.35	402	**0.92**
-7	-5.20	71.05	73	**2.74**	403.68	408	**1.07**
-6	-4.45	78.40	81	**3.32**	408.94	415	**1.48**
-5	-3.71	85.12	88	**3.39**	414.13	422	**1.90**
-4	-2.97	91.34	94	**2.91**	419.26	428	**2.09**
-3	-2.23	97.17	100	**2.91**	424.32	435	**2.52**
-2	-1.48	102.67	106	**3.25**	429.33	441	**2.72**
-1	-0.74	107.88	111	**2.89**	434.28	448	**3.16**
0	0.00	112.86	116	**2.78**	439.17	454	**3.38**
1	0.74	117.62	121	**2.87**	444.01	460	**3.60**
2	1.48	122.20	126	**3.11**	448.80	466	**3.83**
3	2.23	126.62	130	**2.67**	453.54	472	**4.07**
4	2.97	130.88	135	**3.15**	458.23	478	**4.32**
5	3.71	135.01	139	**2.95**	462.87	483	**4.35**
6	4.45	139.02	143	**2.86**	467.46	489	**4.61**
7	5.20	142.92	147	**2.86**	472.01	495	**4.87**
8	5.94	146.71	151	**2.92**	476.52	500	**4.93**
9	6.68	150.41	154	**2.39**	480.98	506	**5.20**
10	7.42	154.01	158	**2.59**	485.40	511	**5.27**

The critical buckling stress values are obtained as 9.53 MPa and 8.61 MPa for Model 1 and Model 4, respectively. When higher stress is induced on the membrane, the imaginary solution is found from Equation 2.2 for mode (0,1). However, the mode (0, 2) is still observed since the effect of the residual stress is less than the fundamental mode. It is also verified by ANSYS harmonic analysis results.

In the absence of the residual stress, the fundamental modes are found as 125 kHz and 116 kHz for Model 1 and Model 4, respectively. In this case, the error between the theoretical results are 1.8% and 2.78%. The fundamental mode frequency reduces by 7.76% due to the holes with 8 μm radius. The resonance frequencies for mode (0,2) are found as 488 kHz and 454 kHz without residual stress. The percentage errors are 2.13 and 3.38.

The effect of the residual stress type is also observed from the simulations. If the membranes experience with the tensile residual stress, the resonance frequencies shift to the higher frequencies. On the other hand, the compressive residual stress reduces the resonance frequency.

The residual stress on the Poly2 layer is reported as -10 MPa by MEMSCAP. According to simulation results, the solid membrane loses the fundamental modes when 10 MPa compressive stress is applied to the Poly2 layer. However, it still exists in Model 4 under favor of the perforation, and it is found as 41 kHz with 64.66% shift. Mode (0,2) is observed in both model under 10 MPa compressive stress. The resonance frequencies for this mode are extracted as 403 kHz and 387 kHz with 1.63% and 0.12% error.

By using Model 1 and Model 4, the advantage of the perforation is investigated. The tabulated data is visualized in Figure 3.3 and Figure 3.4. In order to observe the effect of the hole radius on stress relaxation and resonance frequency, the same procedure is applied to the Model 2 and Model 3. Their hole radii are 4 μm and 6 μm, respectively. The membrane radius is 220 μm as in Model 1 and Model 4. The harmonic analysis results are listed in Table 3.6 and Table 3.7
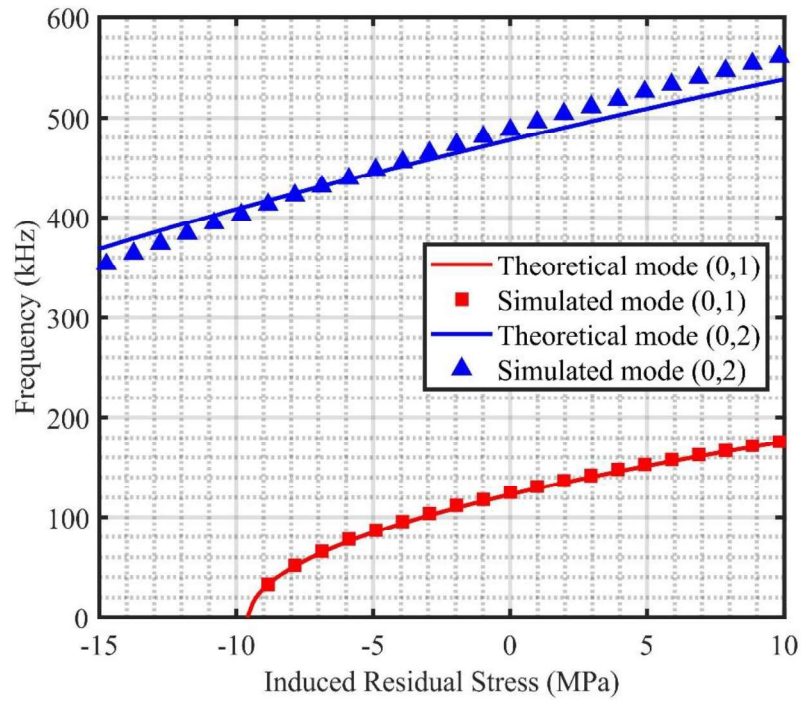
Figure 3.3. Theoretical and simulated resonance mode comparison for Model 1 [36]
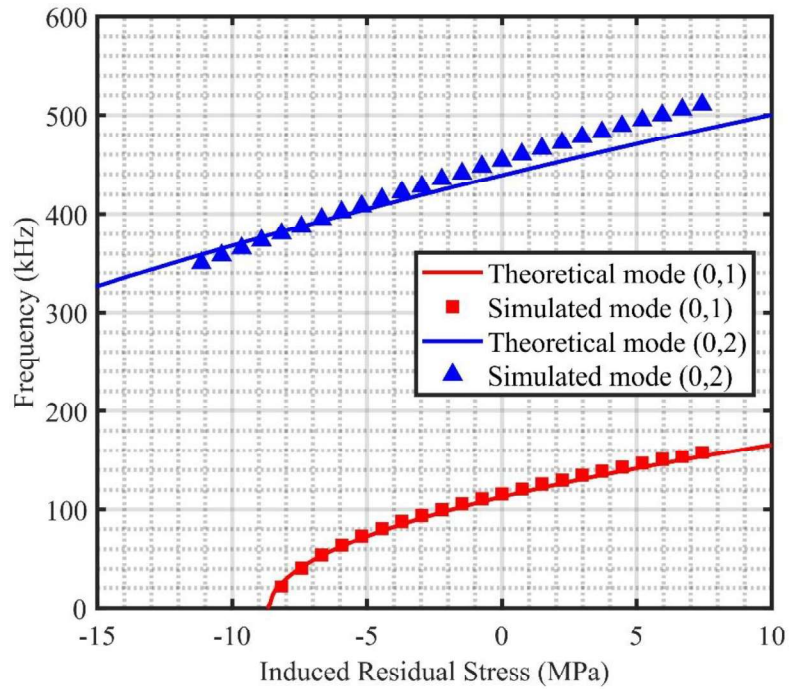
Figure 3.4. Theoretical and simulated resonance mode comparison for Model 4 [36]

Table 3.6. *Harmonic analysis results for Model 2 (membrane radius = 220 μm, hole radius = 4 μm, support = single part)*

Applied Stress (MPa)	Induced Stress (MPa)	Theoretical f(0,1) (kHz)	Simulated f(0,1) (kHz)	Error f(0,1) (%)	Theoretical f(0,2) (kHz)	Simulated f(0,2) (kHz)	Error f(0,2) (%)
-15	-13.69	NA	NA	**NA**	366.16	336	**8.24**
-14	-12.78	NA	NA	**NA**	373.99	346	**7.48**
-13	-11.86	NA	NA	**NA**	381.67	355	**6.99**
-12	-10.95	NA	NA	**NA**	389.19	365	**6.22**
-11	-10.04	NA	NA	**NA**	396.57	374	**5.69**
-10	-9.13	NA	NA	**NA**	403.81	383	**5.15**
-9	-8.21	34.46	33	**4.23**	410.93	392	**4.61**
-8	-7.30	51.74	51	**1.44**	417.92	401	**4.05**
-7	-6.39	64.55	64	**0.86**	424.80	409	**3.72**
-6	-5.48	75.22	75	**0.29**	431.57	418	**3.15**
-5	-4.56	84.54	84	**0.64**	438.24	426	**2.79**
-4	-3.65	92.94	92	**1.01**	444.81	434	**2.43**
-3	-2.74	100.63	100	**0.63**	451.28	442	**2.06**
-2	-1.83	107.78	107	**0.73**	457.66	449	**1.89**
-1	-0.91	114.49	113	**1.30**	463.95	457	**1.50**
0	0.00	120.82	119	**1.51**	470.15	464	**1.31**
1	0.91	126.84	125	**1.45**	476.28	472	**0.90**
2	1.83	132.58	131	**1.19**	482.33	479	**0.69**
3	2.74	138.08	136	**1.51**	488.30	486	**0.47**
4	3.65	143.38	141	**1.66**	494.20	493	**0.24**
5	4.56	148.48	146	**1.67**	500.03	500	**0.01**
6	5.48	153.42	151	**1.58**	505.80	507	**0.24**
7	6.39	158.20	155	**2.02**	511.50	513	**0.29**
8	7.30	162.84	159	**2.36**	517.14	520	**0.55**
9	8.21	167.35	164	**2.00**	522.71	527	**0.82**
10	9.13	171.75	168	**2.18**	528.23	533	**0.90**

Table 3.7. *Harmonic analysis results for Model 3 (membrane radius = 220 μm, hole radius = 6 μm,*
support = single part)

Applied Stress (MPa)	Induced Stress (MPa)	Theoretical f(0,1) (kHz)	Simulated f(0,1) (kHz)	Error f(0,1) (%)	Theoretical f(0,2) (kHz)	Simulated f(0,2) (kHz)	Error f(0,2) (%)
-15	-12.49	NA	NA	**NA**	360.65	338	**6.28**
-14	-11.65	NA	NA	**NA**	367.64	348	**5.34**
-13	-10.82	NA	NA	**NA**	374.51	356	**4.94**
-12	-9.99	NA	NA	**NA**	381.25	365	**4.26**
-11	-9.16	NA	NA	**NA**	387.87	374	**3.58**
-10	-8.32	23.30	21	**9.89**	394.38	382	**3.14**
-9	-7.49	43.05	42	**2.44**	400.79	390	**2.69**
-8	-6.66	56.24	56	**0.42**	407.10	398	**2.23**
-7	-5.83	66.87	67	**0.19**	413.31	406	**1.77**
-6	-4.99	76.03	76	**0.04**	419.43	413	**1.53**
-5	-4.16	84.20	85	**0.95**	425.46	421	**1.05**
-4	-3.33	91.65	92	**0.39**	431.40	428	**0.79**
-3	-2.50	98.53	99	**0.48**	437.27	436	**0.29**
-2	-1.66	104.96	105	**0.03**	443.05	443	**0.01**
-1	-0.83	111.02	112	**0.88**	448.76	450	**0.28**
0	0.00	116.77	117	**0.20**	454.40	457	**0.57**
1	0.83	122.25	123	**0.61**	459.98	463	**0.66**
2	1.66	127.49	128	**0.40**	465.48	470	**0.97**
3	2.50	132.53	133	**0.36**	470.92	477	**1.29**
4	3.33	137.38	137	**0.27**	476.30	483	**1.41**
5	4.16	142.06	142	**0.04**	481.62	490	**1.74**
6	4.99	146.60	146	**0.41**	486.88	496	**1.87**
7	5.83	150.99	151	**0.00**	492.08	502	**2.02**
8	6.66	155.27	155	**0.17**	497.23	508	**2.17**
9	7.49	159.43	159	**0.27**	502.33	515	**2.52**
10	8.32	163.48	163	**0.30**	507.37	521	**2.69**

The critical buckling stress values are found as 8.94 MPa and 8.67 MPa for Model 2 and Model 3, respectively. Although they are higher than Model 4, they are lower than Model 1. It shows that the critical buckling stress decreases with the perforation ratio. The fundamental mode frequency increases with decreasing hole radius. In Model 2, the first resonance frequency is simulated as 119 kHz with 1.51% error in the absence of the residual stress while the mode (0,2) is observed at 464 kHz with 1.31% error. For Model 3, they are found as 117 kHz and 457 kHz with 0.20% and 0.57% errors.

When the residual stress is assumed as -10 MPa, the resonance frequencies shift to 21 kHz and 382 kHz with 9.89% and 3.14% deviation from theoretical calculations for Model 3. The first resonance frequency extraction has high deviation since the residual stress is -8.32 MPa which is close to its buckling stress value. In this region, the resonance frequency is strongly dependent on the induced stress. The frequency step size (1 kHz) has a crucial effect on the resonance frequency extraction and error calculation. Like Model 1, the buckling is observed under 10 MPa compressive stress for Model 2, and the first mode vanishes. From this point of view, holes with 4 μm radius do not provide required stress relaxation to prevent buckling. On the other hand, the mode (0,2) is observed at 383 kHz with 5.15% error.

The effect of the tensile stress is also clearly observed for Model 2 and 3. Under high tensile stress, the resonance frequencies significantly increase. The first resonance frequencies are found as 168 kHz and 163 kHz, respectively. They are shifted by 41.18% and 39.32%.

Through the Model 2, 3 and 4, the effects of the hole radius are investigated. Although the critical buckling stress is reduced with increasing hole radius, the durability under higher stress values is improved with higher stress relaxation. The tabulated data is visualized in Figure 3.5 and Figure 3.6. Furthermore, Model 5 and 8, which are identical to fabricated Design A and B, are simulated and harmonic analysis results are shown in Table 3.8 and Table 3.9.
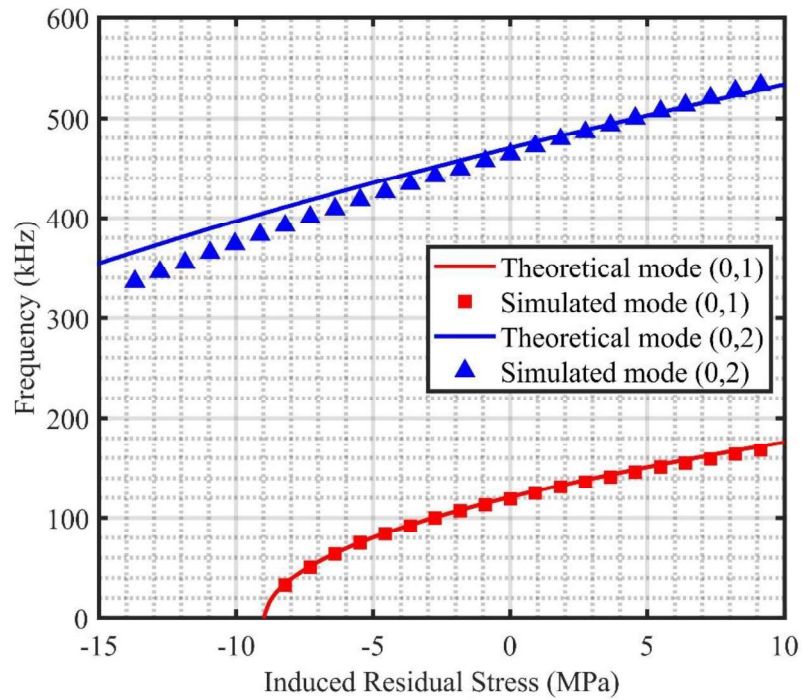
*Figure 3.5.* Theoretical and simulated resonance mode comparison for Model 2 [36]
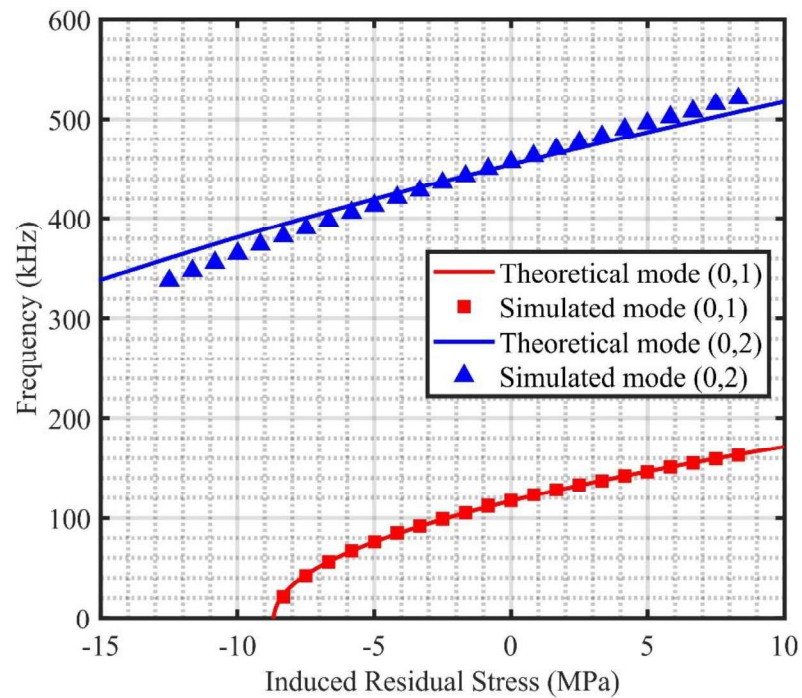
Figure 3.6. Theoretical and simulated resonance mode comparison for Model 3 [36]

Table 3.8. *Harmonic analysis results for Model 5 (membrane radius = 220 μm, hole radius = 8 μm, support = four parts)*

Applied Stress (MPa)	Induced Stress (MPa)	Theoretical f(0,1) (kHz)	Simulated f(0,1) (kHz)	Error f(0,1) (%)	Theoretical f(0,2) (kHz)	Simulated f(0,2) (kHz)	Error f(0,2) (%)
-15	-9.99	NA	NA	**NA**	364.49	334	**8.36**
-14	-9.32	NA	NA	**NA**	369.94	340	**8.09**
-13	-8.66	NA	NA	**NA**	375.31	347	**7.54**
-12	-7.99	20.02	16	**20.10**	380.62	354	**6.99**
-11	-7.33	37.76	36	**4.66**	385.82	360	**6.69**
-10	-6.66	49.54	48	**3.10**	390.97	366	**6.39**
-9	-5.99	59.01	58	**1.71**	396.06	372	**6.07**
-8	-5.33	67.16	66	**1.73**	401.08	378	**5.75**
-7	-4.66	74.42	74	**0.57**	406.03	384	**5.43**
-6	-4.00	81.04	80	**1.28**	410.93	390	**5.09**
-5	-3.33	87.15	86	**1.32**	415.77	396	**4.76**
-4	-2.66	92.86	92	**0.93**	420.56	402	**4.41**
-3	-2.00	98.24	97	**1.27**	425.29	407	**4.30**
-2	-1.33	103.35	102	**1.30**	429.97	413	**3.95**
-1	-0.67	108.21	107	**1.11**	434.59	418	**3.82**
0	0.00	112.86	112	**0.76**	439.17	424	**3.46**
1	0.74	117.33	116	**1.13**	443.71	429	**3.31**
2	1.48	121.63	120	**1.34**	448.19	434	**3.17**
3	2.23	125.78	124	**1.42**	452.64	439	**3.01**
4	2.97	129.81	128	**1.39**	457.03	444	**2.85**
5	3.71	133.71	132	**1.28**	461.39	449	**2.69**
6	4.45	137.50	136	**1.09**	465.71	452	**2.94**
7	5.20	141.19	139	**1.55**	469.98	455	**3.19**
8	5.94	144.79	143	**1.23**	474.22	458	**3.42**
9	6.68	148.30	146	**1.55**	478.42	468	**2.18**
10	7.42	151.72	149	**1.80**	482.59	472	**2.19**

Table 3.9. *Harmonic analysis results for Model 8 (membrane radius = 205 μm, hole radius = 8 μm,*
support = four parts)

Applied Stress (MPa)	Induced Stress (MPa)	Theoretical f(0,1) (kHz)	Simulated f(0,1) (kHz)	Error f(0,1) (%)	Theoretical f(0,2) (kHz)	Simulated f(0,2) (kHz)	Error f(0,2) (%)
-15	-9.96	NA	NA	**NA**	431.12	383	**11.16**
-14	-9.21	16.23	23	**41.68**	437.16	392	**10.33**
-13	-8.63	36.25	32	**11.72**	441.81	396	**10.37**
-12	-7.97	50.12	47	**6.22**	447.06	402	**10.08**
-11	-7.30	60.91	58	**4.78**	452.24	408	**9.78**
-10	-6.64	70.06	67	**4.37**	457.37	414	**9.48**
-9	-5.98	78.15	75	**4.03**	462.44	420	**9.18**
-8	-5.31	85.47	82	**4.07**	467.46	426	**8.87**
-7	-4.65	92.22	89	**3.49**	472.42	432	**8.56**
-6	-3.98	98.50	95	**3.56**	477.33	438	**8.24**
-5	-3.32	104.41	101	**3.27**	482.19	443	**8.13**
-4	-2.66	110.00	107	**2.73**	487.00	449	**7.80**
-3	-1.99	115.32	112	**2.88**	491.77	454	**7.68**
-2	-1.33	120.40	117	**2.83**	496.49	460	**7.35**
-1	-0.66	125.28	121	**3.42**	501.16	465	**7.22**
0	0.00	129.98	126	**3.06**	505.80	470	**7.08**
1	0.66	134.51	130	**3.35**	510.39	475	**6.93**
2	1.33	138.89	134	**3.52**	514.93	480	**6.78**
3	1.99	143.14	138	**3.59**	519.44	485	**6.63**
4	2.66	147.27	142	**3.58**	523.91	490	**6.47**
5	3.32	151.28	146	**3.49**	528.35	495	**6.31**
6	3.98	155.20	150	**3.35**	532.74	499	**6.33**
7	4.65	159.01	154	**3.15**	537.10	503	**6.35**
8	5.31	162.73	157	**3.52**	541.42	507	**6.36**
9	5.98	166.38	161	**3.23**	545.72	511	**6.36**
10	6.64	169.94	164	**3.50**	549.97	514	**6.54**

The support with four parts affects the resonance frequencies by providing higher stress relaxation than the support with single part. Their critical buckling stress values are 8.25 MPa and 9.36 MPa with 33.39% relaxation. Thus, they are not buckled up to 12.38 MPa and 14.05 MPa, respectively.

Under 10 MPa compressive stress, the resonance frequencies are extracted as 48 kHz and 366 kHz for Model 5 (Design A). They are found as 67 kHz and 414 kHz for Model 8 (Design B).

In harmonic analysis, the effects of the perforation and residual stress are investigated. From the ten ANSYS models, only one of them has an error greater than 5%. The achieved smallest percentage error is 0.52 among the ten configurations. The models which consist of a support structure with four symmetric parts are the most deviated ones since they are assumed to have clamped supports in analytical calculations. However, they are slightly different from the clamped boundary conditions. Average percentage errors are listed in Table 3.10.

Table 3.10. *Percentage error of the resonance frequency extraction on ANSYS [36]*

Model Number	*Percentage Error of Mode (0,1) (%)*	*Percentage Error of Mode (0,2) (%)*
1	2.03	2.45
2	1.51	2.78
3	0.89	2.16
4	3.26	2.77
5	2.33	4.62
6	0.56	1.93
7	2.51	2.76
8	0.52	1.83
9	3.13	2.09
10	5.46	7.94

3.2. Electrical Simulations

Electrical simulations are carried out using Agilent Advanced Design System and Electro Magnetic Professional (ADS & EMPro 2020, Keysight Technologies, California). These tools can be used to extract electrical parameters of the membranes via electromagnetic analogy. Through the ADS-EMPro simulations, similar parameters provided by network analyzer are acquired.

3.2.1. Model Generation for Electrical Simulations

In ADS, the models are constructed based on the stack principle. The layers and their thicknesses are defined in the stack. They are generated according to the positions on the stack. Depending on PolyMUMPs layer configuration, the following stack is created and used in the electrical simulations.

Figure 3.7. Constructed stack in ADS

In microfabrication, the gap between Poly2 and Poly0 layers is determined by the sacrificial oxide layer thicknesses which are 2 µm and 0.75 µm. Thus, the fabricated devices have an air gap with 2.75 µm. In order to achieve the required air gap, the Poly1 layer thickness is taken as 2.75 µm. Furthermore, electrical parameters are set as shown in Table 3.11.

Table 3.11. *Electrical parameters of the materials used in ADS*

Layer	Resistivity (Ω-cm)	*Relative Permittivity (ε_r)*
Substrate	1	11.9
Nitride	-	8.5
Poly0	1.5×10^{-3}	-
Poly1	2.0×10^{-3}	-
Poly2	3.0×10^{-3}	-
Gold	2.4×10^{-5}	-

Based on these properties, the ADS model is generated with the fabrication masks which are imported from L-Edit. Ground and signal electrodes are defined to specify the ports where the electrical parameters are found. To improve the accuracy of simulations, the composed models are exported to EMPro since ADS is specialized for the frequencies in the MHz range.

The exported models are meshed and simulated in the frequency range 1 kHz to 500 kHz with EMPro. From these simulations, the series resistance and capacitances are calculated for each design.

3.2.2. Electrical Simulation Results and Discussions

For 2.75 μm air gap, the series capacitances are observed as 26.76 pF and 26.31 pF at 500 kHz for Design A and Design B, respectively. The series resistances are found as 49.55 Ω and 50.53 Ω.
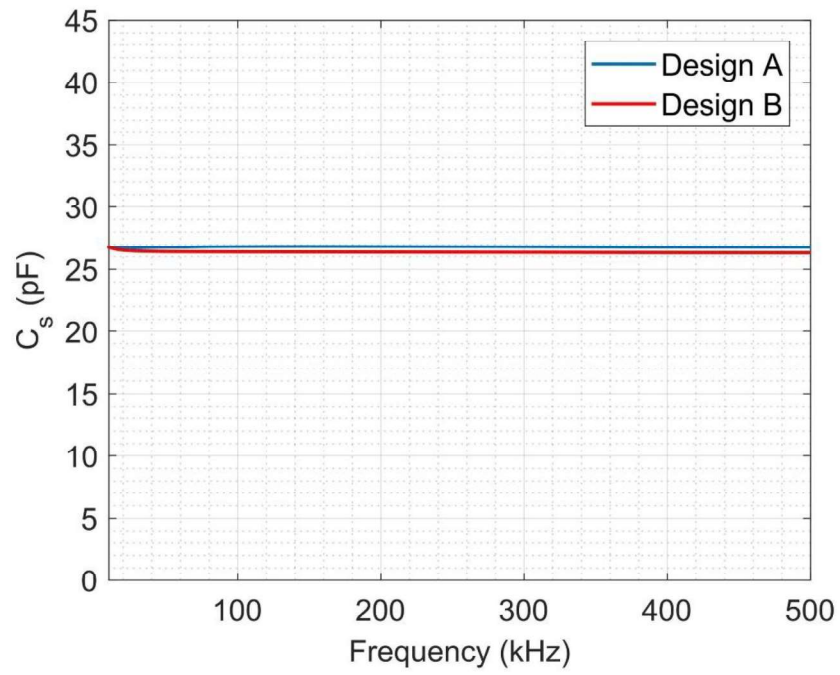
(a)
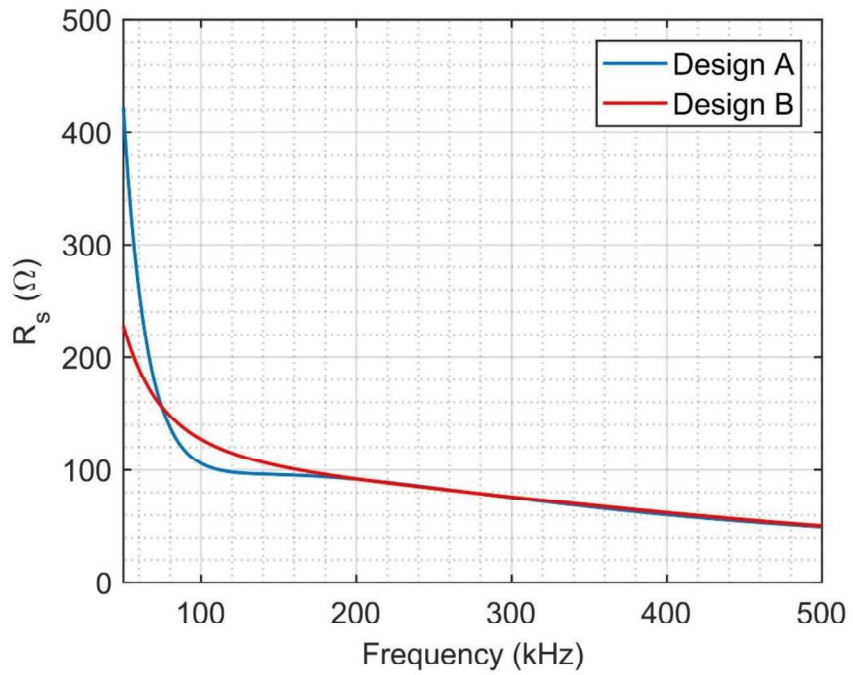
(b)

Figure 3.8. Simulated series capacitance and resistance values for proposed designs

The impedance extractions are not accurate at low frequencies due to the drawback of EMPro solver. Furthermore, the air gap is swept from 2.75 µm to 0.06 µm in ADS simulations to find parallel plate capacitance as a function of gap distance. The total capacitance is assumed as in Equation 3.1. From ADS simulations, the parasitic capacitances are found as 26.54 pF and 26.21 pF for Design A and Design B, respectively. Also, the parallel plate capacitances are obtained as 0.76 pF-µm and 0.65 pF-µm

$$C_s(gap) = C_{s_{parasitic}} + \frac{C_{s_{parallel}}}{gap} \tag{3.1}$$
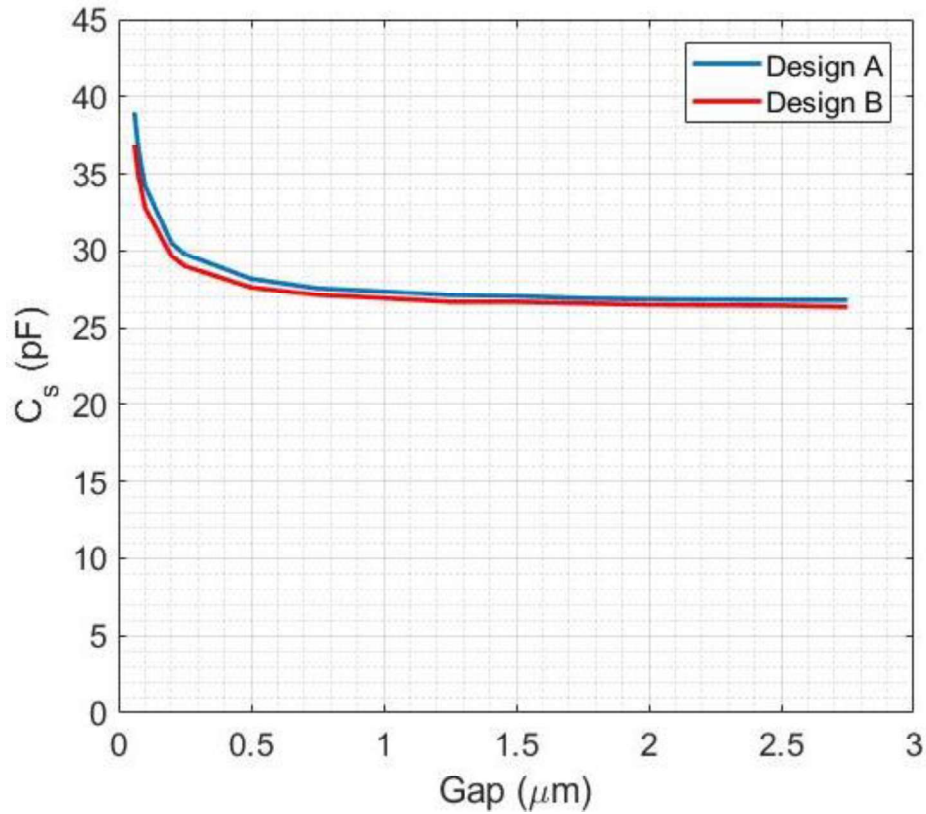
Figure 3.9. Series capacitance extraction of the proposed designs as a function of gap

CHAPTER 4

EXPERIMENTAL WORK

4.1. Optical Measurements

4.1.1. Optical Measurement Setup Configuration

For the experimental measurements, the fabricated membranes are placed to the chip carrier and the electrical connections between gold lines on the chip carrier and electrical pads of the membrane are provided via gold wire bonds. Through the chip carrier, the membrane can be excited electrically via SMA (SubMiniature version A). The fabricated membranes are characterized under the optical measurement setup shown in Figure 4.1.
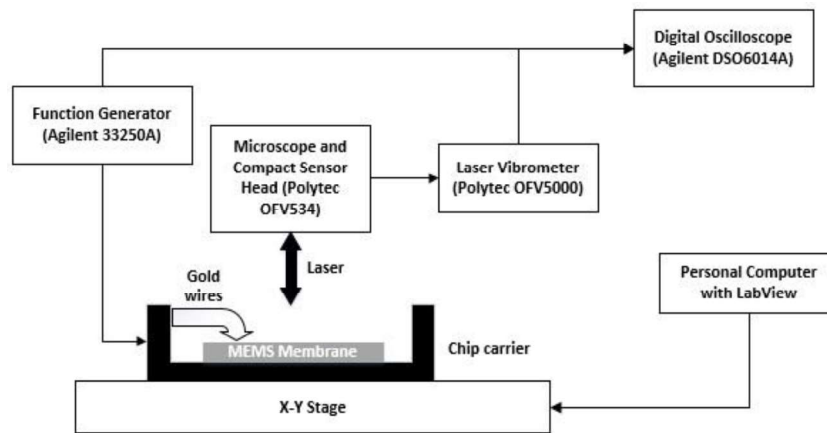

Figure 4.1. Optical characterization setup

The optical setup is based on the membrane deflection with the applied electrical excitation. The LabView software (National Instruments, USA) controls the X-Y stage to focus the laser from Compact Sensor Head (OFV534, Polytec, Germany) onto the membrane. Function Generator (33250A, Agilent, USA) is used both for DC biasing and AC excitation source. The sensor head transmits the laser light and collects

the reflected light from membrane. Laser Vibrometer (OFV5000, Polytec, Germany) decodes sensor head's signal. The laser vibrometer's output is observed in Digital Oscilloscope (DSO6014A, Agilent, USA).

By using the depicted optical setup, velocity measurement is performed with VD-09 decoder. It generates a sinusoidal signal output with 20 mm/s/V range. The maximum operating frequency is 1 MHz. They are excited with 0.1 V peak-to-peak sinusoidal signal with 0.75 V, 1.25 V, 1.75 V DC bias. The optical measurements are performed for 16 and 14 data points for Design A and Design B, respectively as shown in Figure 4.2 and Figure 4.3, respectively. The frequency of the sinusoidal signal is swept from 5 kHz to 500 kHz. In this way, the overall response of the membrane is comprehended in terms of both radial position and frequency.
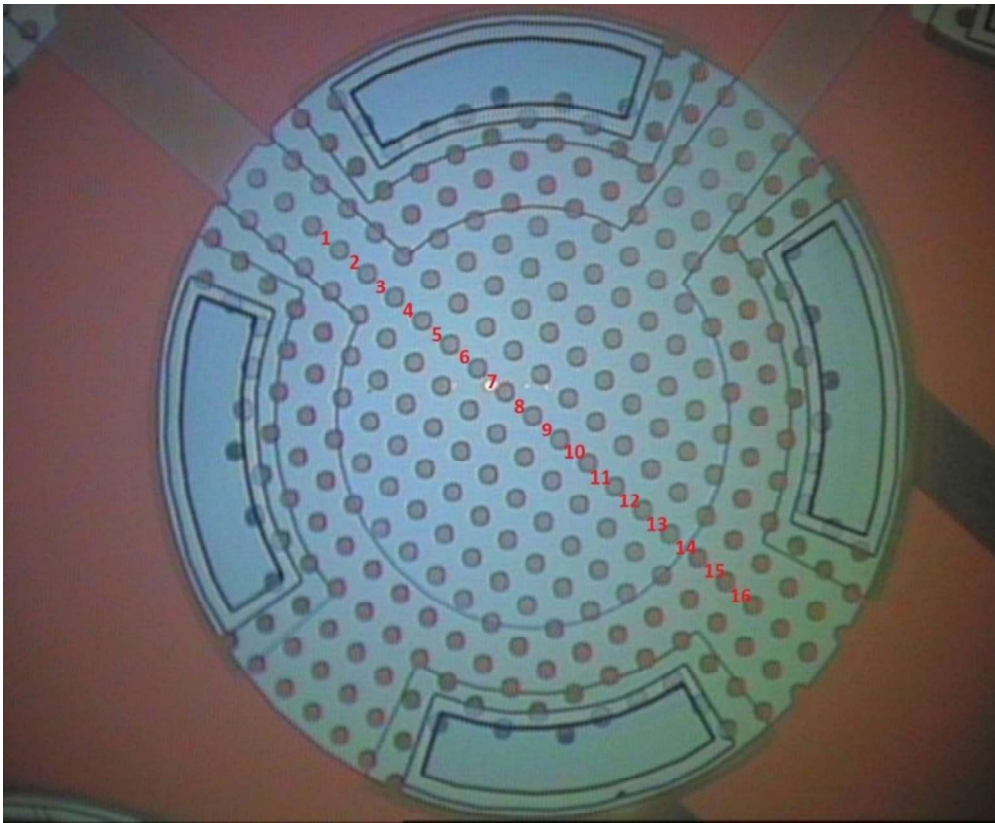

*Figure 4.2.* Microscope view and optical measurement data points of Design A
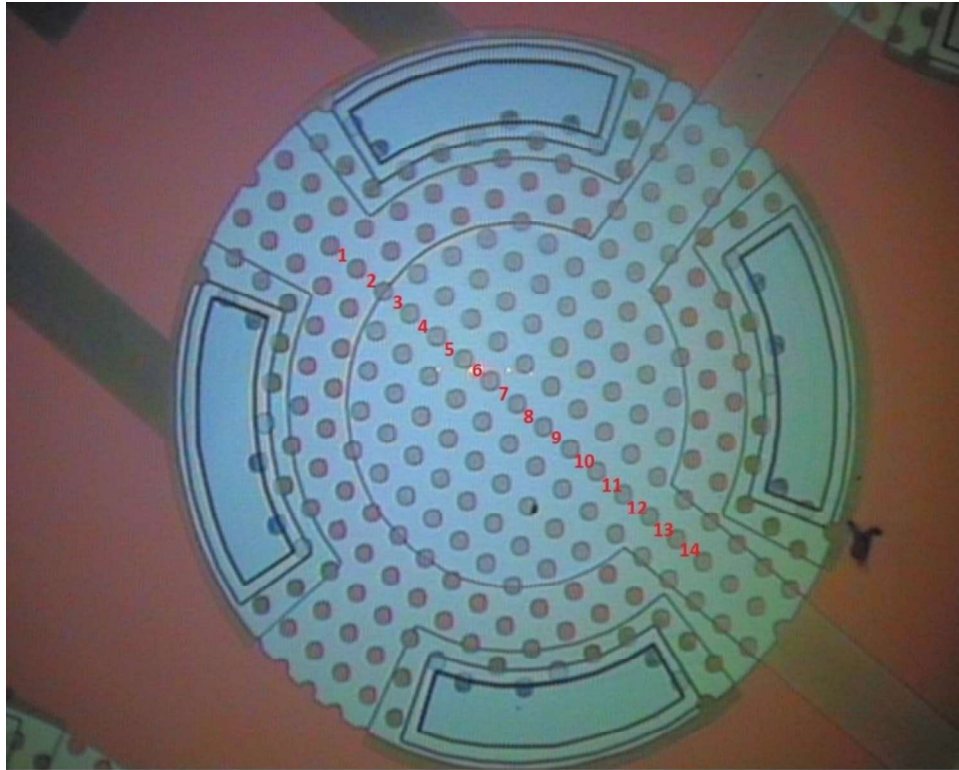
Figure 4.3. Microscope view and optical measurement data points of Design B

4.1.2. Optical Measurement Results and Discussions

The deflection characteristic of the membranes is acquired from velocity output of the vibrometer under different DC bias values. The obtained velocity outputs are converted to the displacement by using decoder range (20 mm/s/V). As shown in Figure 4.4, the displacement data obtained from maximum DC bias (1.75 V) is normalized to clearly observe the vibrational modes of the membrane. The negative radial positions correspond to lower data points, the positive ones are the higher data points. For the first mode, the maximum displacement occurs at 25 kHz and 40 kHz for Design A and Design B, respectively. The maximum displacement for the second mode is observed at 285 kHz and 335 kHz.
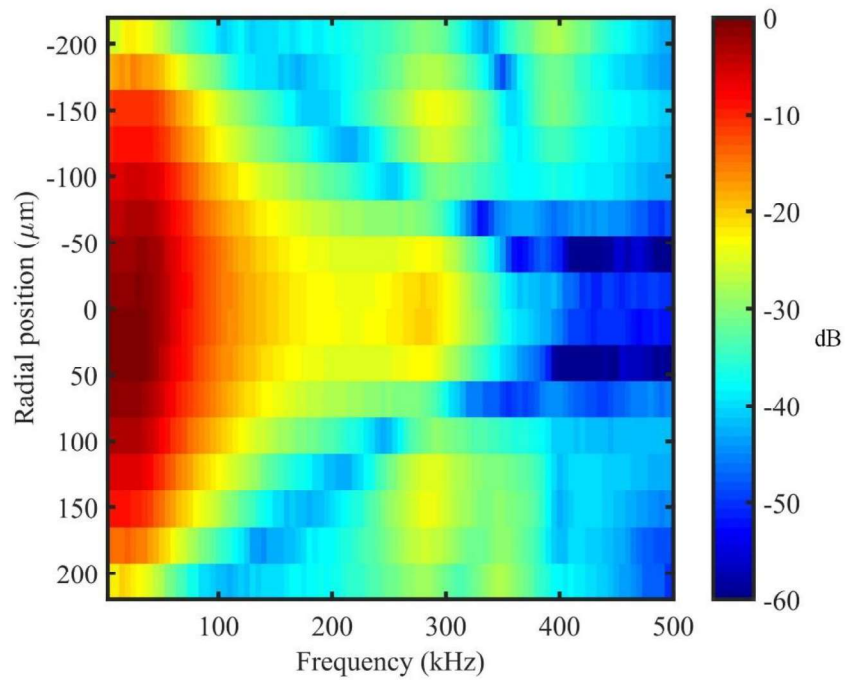
(a)
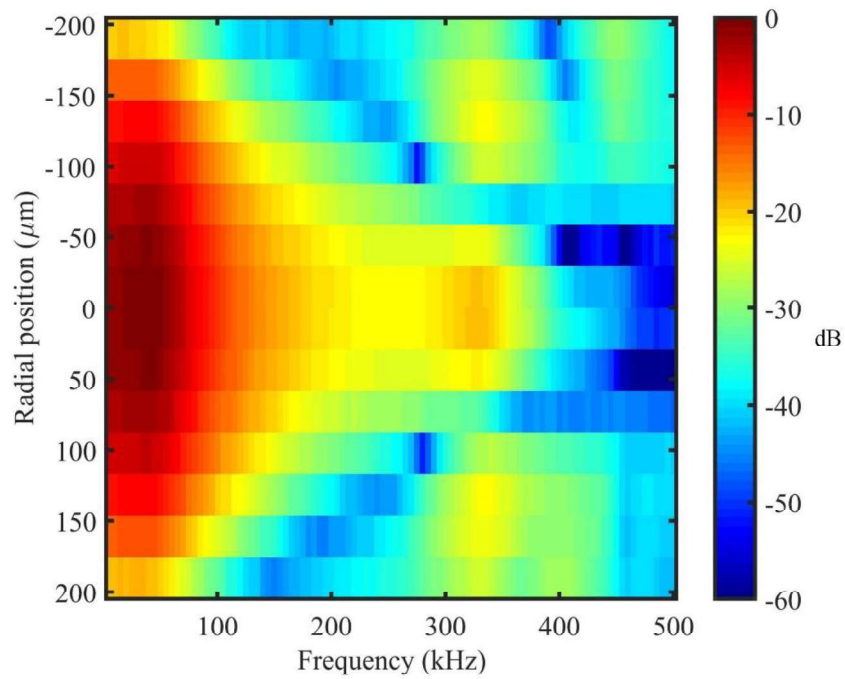
(b)

Figure 4.4. Normalized displacement for (a) Design A, (b) Design B under 1.75 V DC bias [36]

Displacement characteristics of the selected data points under 1.75 V DC bias are shown in Figure 4.5 and Figure 4.6 to clearly observe the symmetrical response through the radial positions.
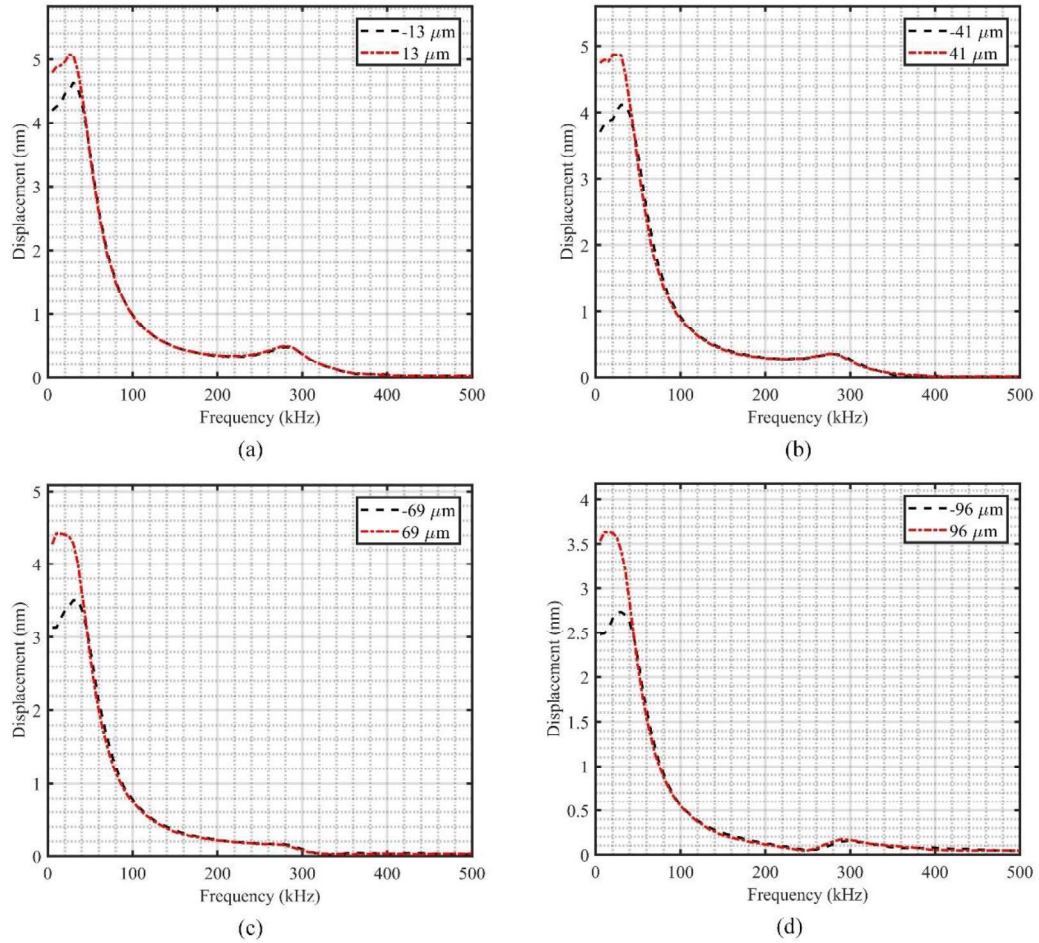

Figure 4.5. Displacement at (a) 13 μm, (b) 41 μm, (c) 69 μm, (d) 96 μm for Design A under 1.75 V DC bias

For Design A, the positive data points have more deflection than the negative data points at the lower frequencies. The symmetry axis of the first mode is shifted to the positive side. On the other hand, the displacement characteristics of the central symmetric data points are perfectly matched above 60 kHz.
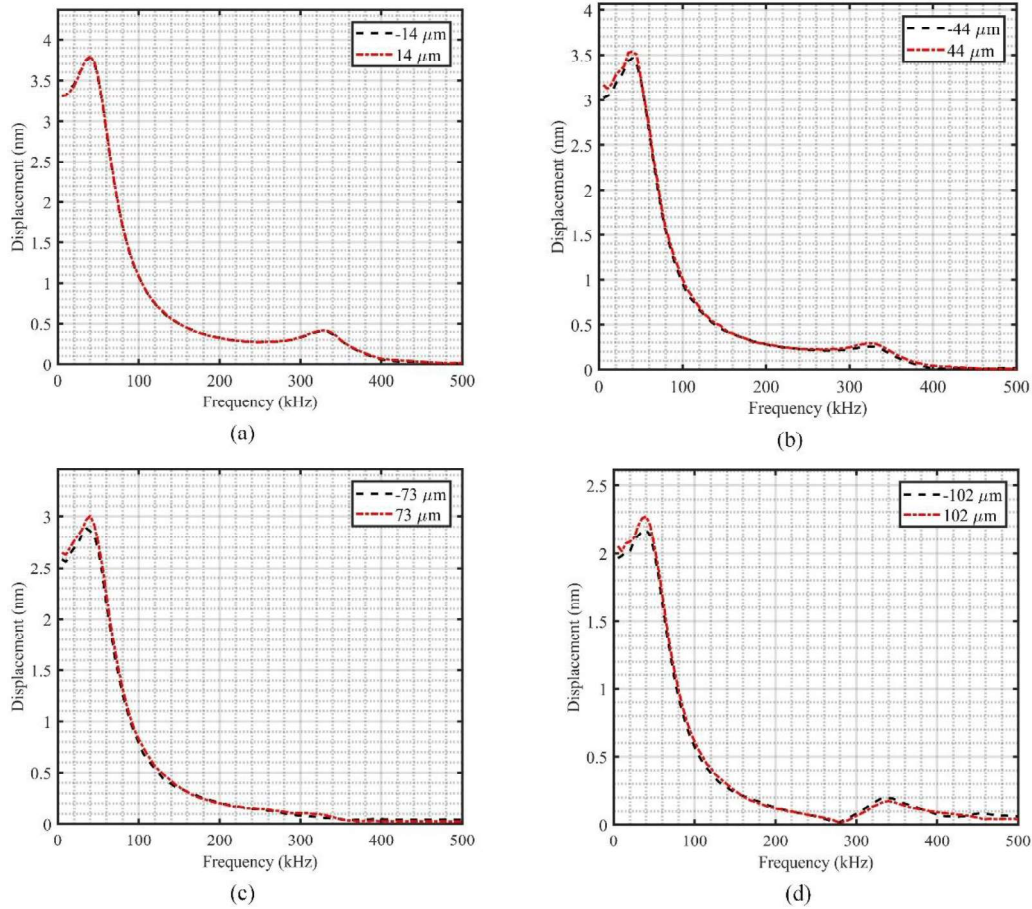
Figure 4.6. Displacement at (a) 14 µm, (b) 44 µm, (c) 73 µm, (d) 102 µm for Design B under 1.75 V DC bias

Unlike Design A, the central symmetry is achieved for the first mode in addition to the second mode. The small differences may be caused by the laser point adjustment errors since it is not possible to point the laser at exactly symmetric locations.

By the help of the normalized displacement, the frequencies where the maximum deflection is observed on the vibrational modes are determined. At those frequencies, first and second mode shapes are extracted for the proposed designs. It can be seen from Figure 4.7.
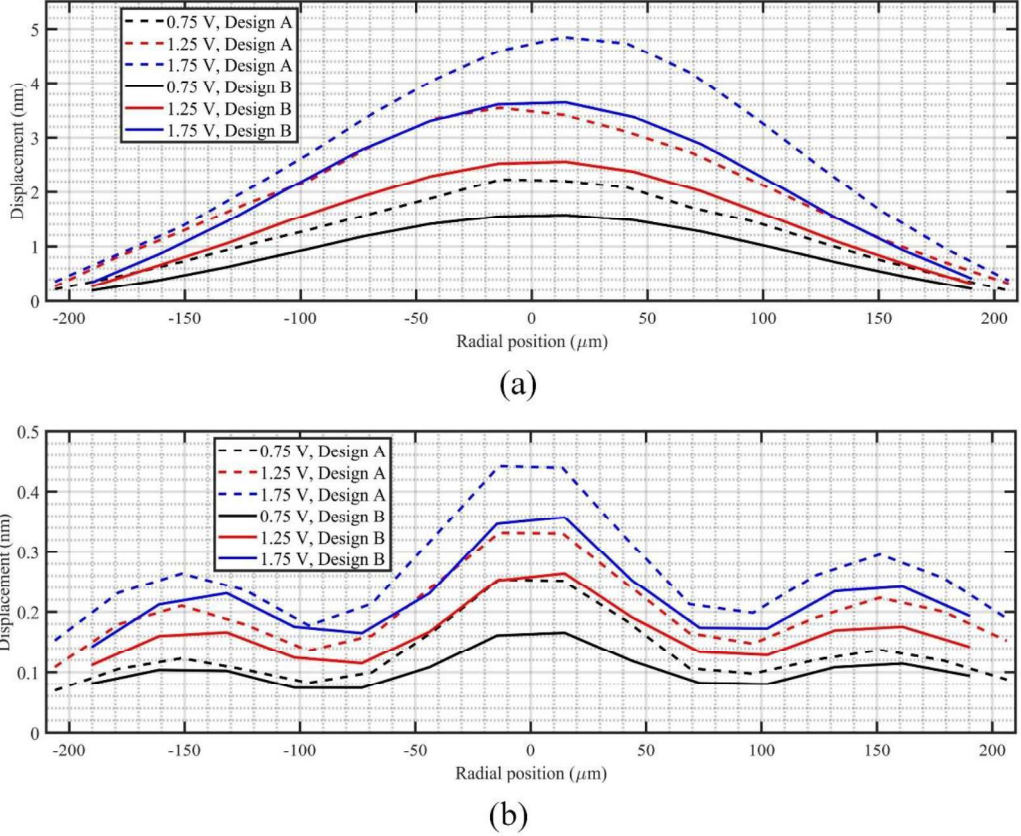
*Figure 4.7.* (a) Mode (0,1), (b) Mode (0,2) shapes under different DC bias

Through the optical measurements, the deflection profiles of the pre-stressed membranes are found out under different DC bias values. Figure 4.4 and Figure 4.7 indicate the central symmetry of the membranes. As it is seen from Figure 4.4, the maximum displacement appears at the center points for both first and second modes. In addition to central symmetry, Figure 4.7 implies that the first mode is deflected approximately ten times more than second mode. It shows that the first mode is more dominant. With the increasing DC bias, the membrane deflection also increases due to the electrostatic force between membrane and ground plate.

As shown in Figure 4.8, maximum deflection at center point for Design A and B is found out 5.07 nm at 25 kHz and 3.8nm at 40 kHz, respectively. The maximum average displacement of the membranes is determined as 1.8 nm at 25 kHz and 1.48

nm at 40 kHz. Furthermore, the secondary peaks are recognized in deflection profiles at 285 kHz and 335 kHz.
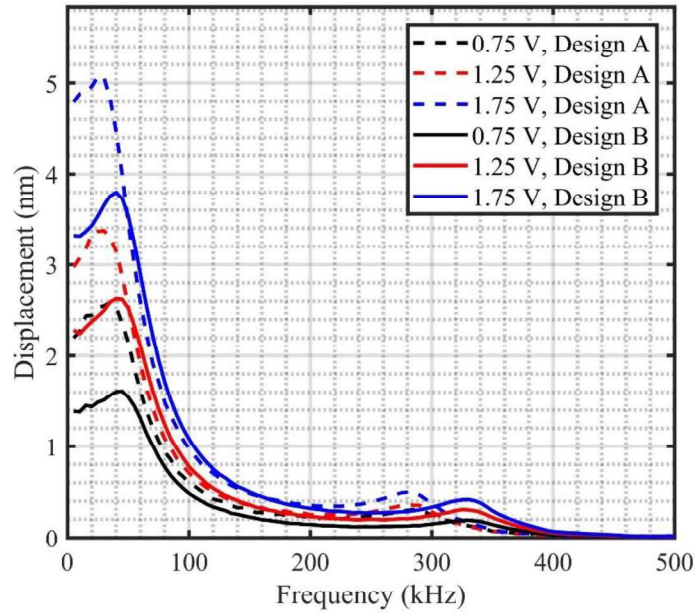

(a)
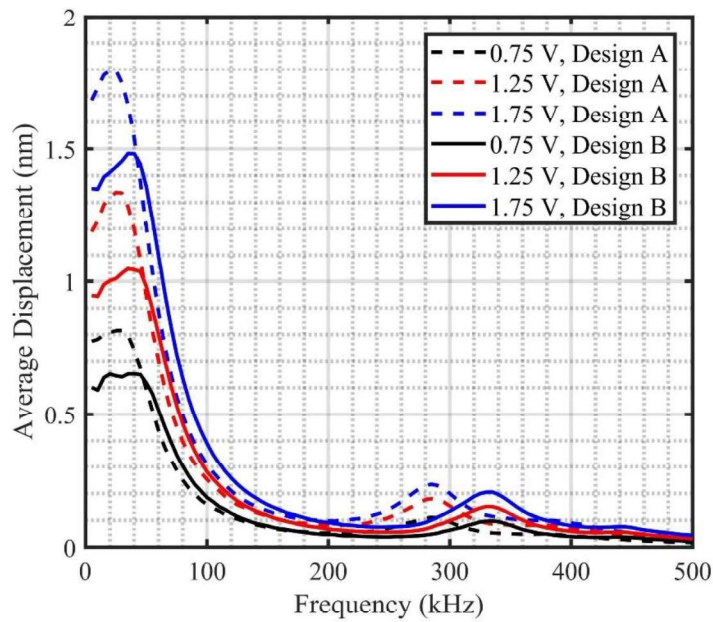
(b)

Figure 4.8. (a) Membrane displacement at the center point, (b) Membrane average displacement under different DC bias [36]

Figure 4.8 indicates the displacement characteristic of the membranes depending on the DC bias. The membranes are stable against to DC bias alteration. Although the displacement substantially increases with the DC bias, the spring softening domination is not inspected. It emphasizes that the operated DC bias values are not close to the collapse voltages of the designs.

The average displacement on the membrane is crucial since the membrane is assumed as a parallel plate capacitor. For the parallel plate assumption, the single point deflection is not enough to calculate the capacitance changes. Thus, results of the selected data points are evaluated to calculate the average displacement. Furthermore, the displacement on Design A is greater than Design B since the larger radius causes smaller mechanical stiffness. Therefore, Design B is stiffer to the bending against to electrostatic forces.

In order to determine the resonance frequencies of the membranes, the output pressure is calculated. It is proportional to velocity of the membrane. Thus, the velocity output of the vibrometer is normalized based on the first resonance frequencies and plotted in Figure 4.9. The resonance frequencies are found as 45 kHz, 285 kHz for Design A and they are 55 kHz and 335 kHz for Design B.

For both fabricated designs, the resonance frequencies do not changed with DC bias. It means there are no effective spring softening effects on these voltage values. The pressure is obtained by multiplying membrane output velocity and acoustical impedance of the air. Then, it is normalized based on the first resonance frequencies since the acoustic impedance of the second mode is smaller than the first mode. For the calculation simplicity, the acoustical impedances are assumed as the same.
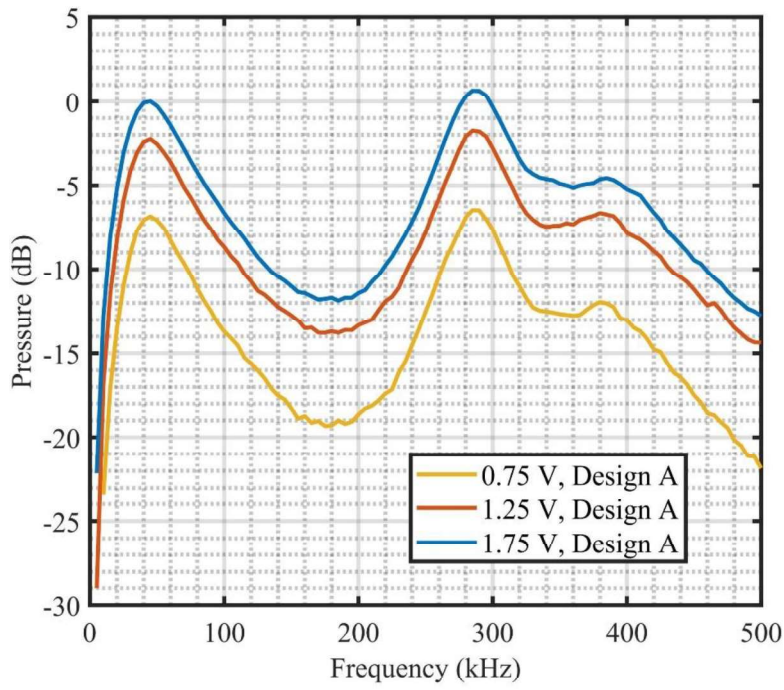
(a)
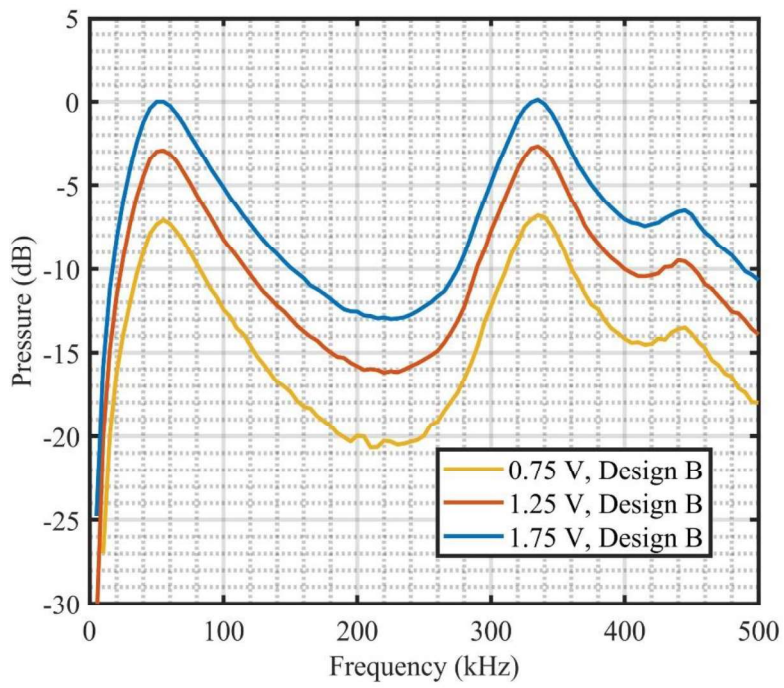
(b)

Figure 4.9. Normalized pressure output for (a) Design A, (b) Design B [36]

62

All in all, the critical values obtained from laser vibrometer measurements are listed in Table 4.1. Measured displacement data cannot be compared with ANSYS simulations since the membrane is mechanically excited by applying pressure in ANSYS simulations. However, it is possible to compare resonance frequencies that are based on the normalized displacement data.

Table 4.1. *Maximum displacement and resonance frequencies for the fabricated membranes under different DC bias values*

Design	DC Bias	Maximum Average Displacement, Frequency	Maximum Displacement at Center, Frequency	First & Second Resonance Frequency from Pressure Measurement
A	1.75 V	1.8 nm, 25 kHz	5.08 nm, 25 kHz	45 kHz, 285 kHz
A	1.25 V	1.34 nm, 30 kHz	3.37 nm, 30 kHz	45 kHz, 285 kHz
A	0.75 V	0.82 nm, 30 kHz	2.55 nm, 30 kHz	45 kHz, 285 kHz
B	1.75 V	1.48 nm, 35 kHz	3.8 nm, 40 kHz	55 kHz, 335 kHz
B	1.25 V	1.05 nm, 35 kHz	2.62 nm, 40 kHz	55 kHz, 335 kHz
B	0.75 V	0.65 nm, 40 kHz	1.61 nm, 45 kHz	55 kHz, 335 kHz

4.2. Electrical Measurements

4.2.1. Electrical Measurement Setup Configuration

Electrical characterization of the fabricated devices is performed with network and impedance analyzer (5061B, Keysight Technologies, California, USA). The series through method is used with gain phase mode via LF Out port as shown in Figure 4.10. The 10% accuracy range is about 5 Ohm to 20 kΩ for this method [37].
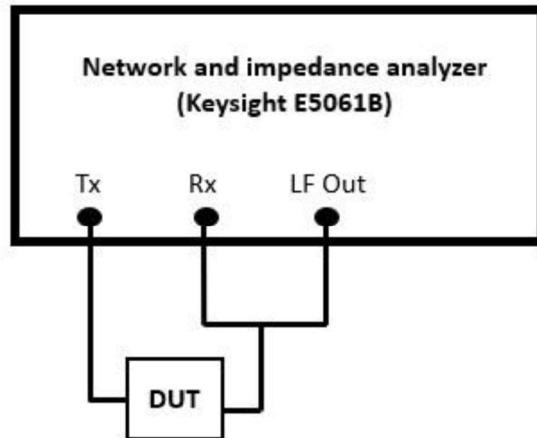
Figure 4.10. Electrical measurement setup

In order to extract series resistance (R_s) and series capacitance (C_s) values, the frequency range is chosen as 1 kHz to 500 kHz. In addition, Intermediate Frequency Band Width (IFBW) is set to 1 kHz with an averaging of 16. -10dBm (100 mV peak-to-peak) sinusoidal signal is applied with DC bias changing from 0 V to 1.75 V. 1601 data points are taken in the given frequency range. Also, open/short/load (50 Ω) calibrations are performed to acquire higher accuracy from the impedance measurements.

4.2.2. Electrical Measurement Results and Discussions

The electrical measurements are carried out with gain phase series setup for 0 V, 0.75 V, 1.25 V and 1.75 V DC bias values with 100 mV peak-to-peak sinusoidal signal. The measured C_s and R_s values are shown in Figure 4.12 and Figure 4.13, respectively. There is no significant change on impedance values depending on the applied DC bias and excitation frequency. The series capacitances are measured as 40.04 pF and 39.80 pF under 1.75 DC bias at 500 kHz for Design A and Design B, respectively. Under the same conditions, the series resistance values are observed as 54.63 Ω and 50.87 Ω.
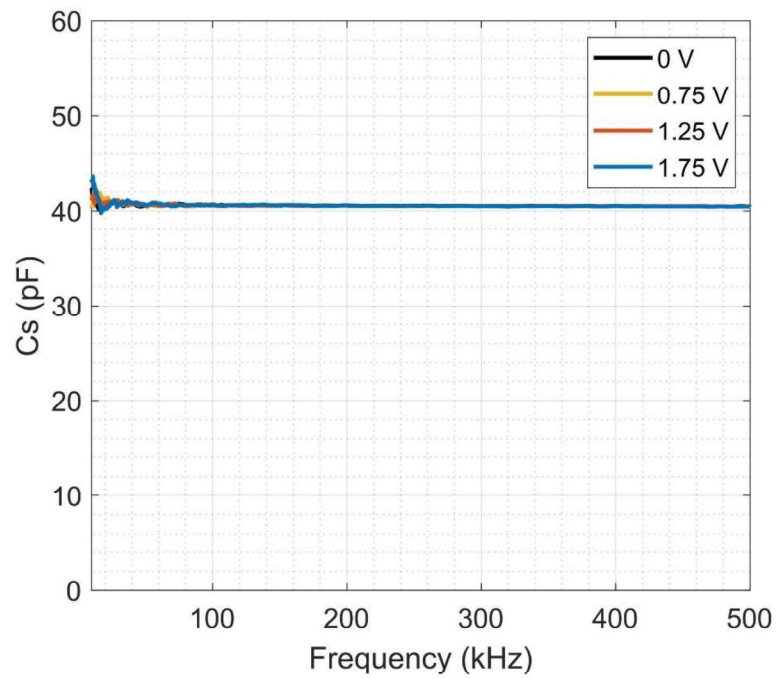
(a)
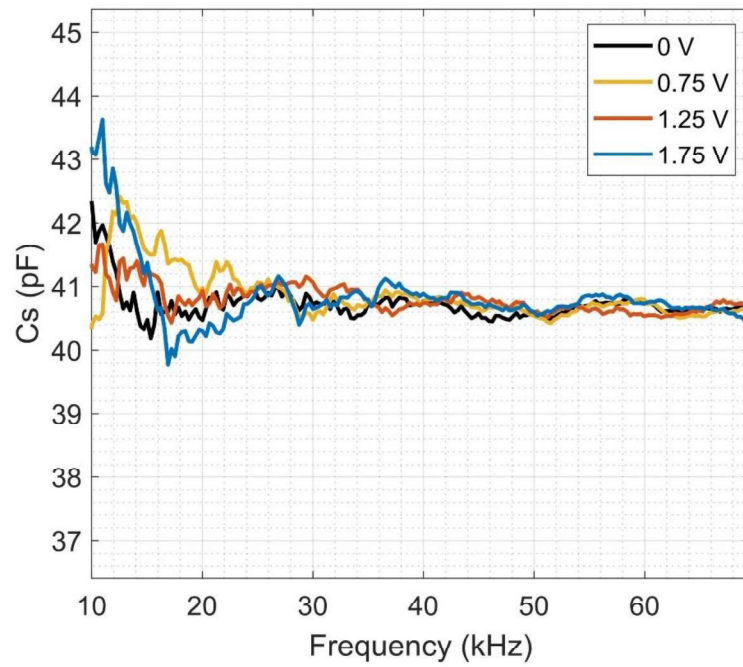
(b)

*Figure 4.11.* Measured series capacitance for Design A, (b) zoomed in low frequencies
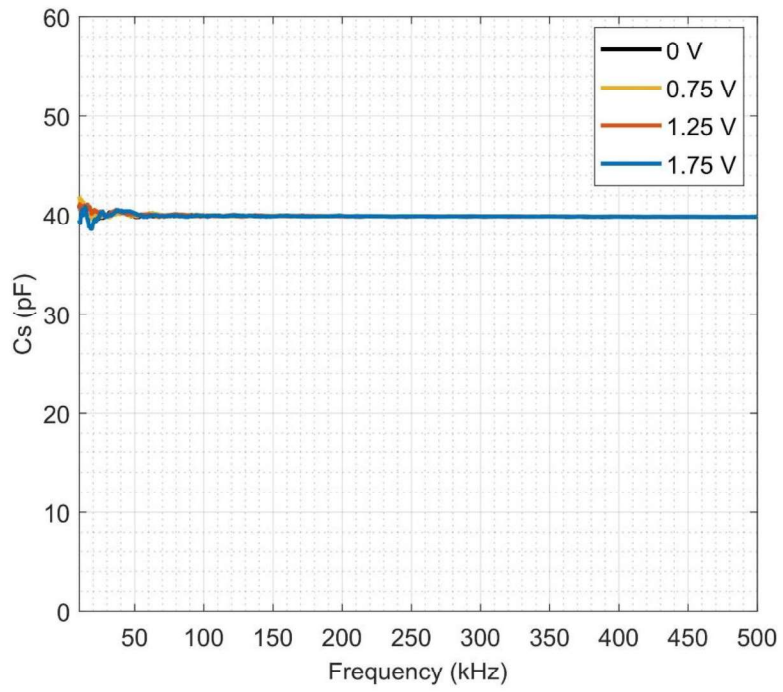
(a)
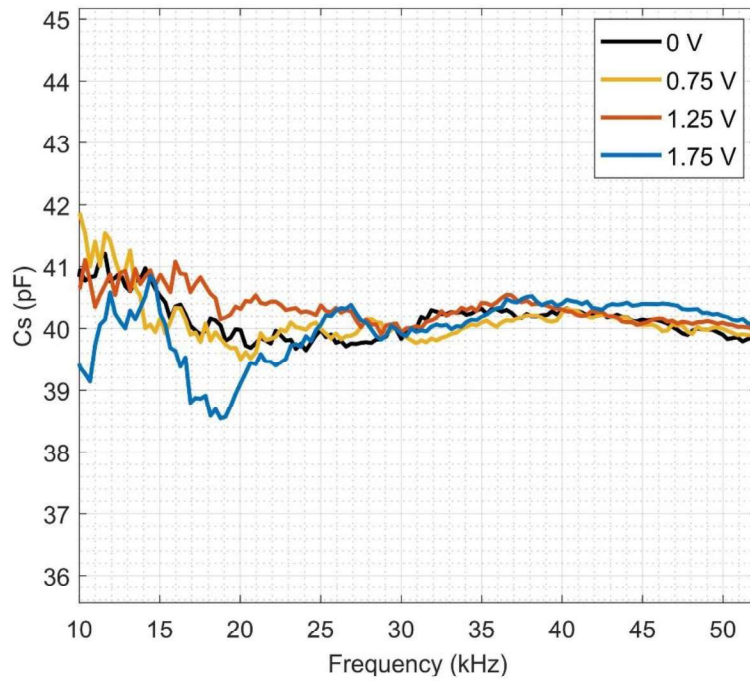
(b)

Figure 4.12. (a) Measured series capacitance for Design B, (b) zoomed in low frequencies
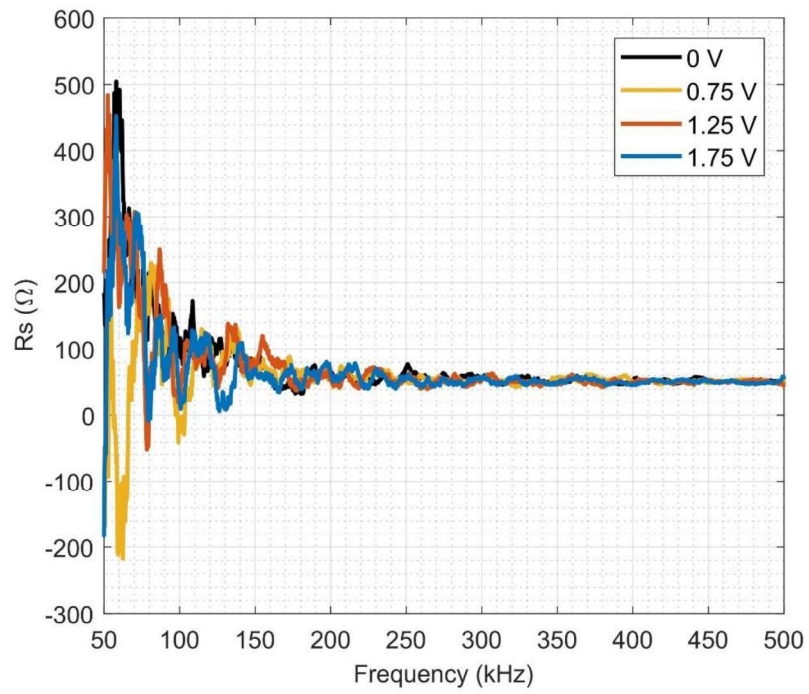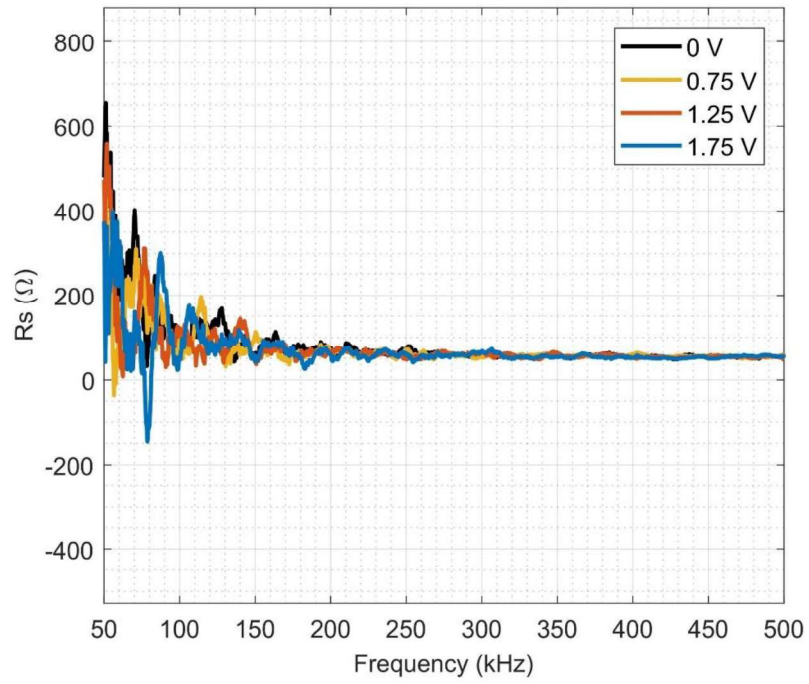
Figure 4.13. (a) Measured series resistance for Design A, (b) Design B

The series capacitances are around 40 pF for different DC bias values. There is no significant change in the capacitance with increasing DC bias due to the small deflections of the membrane compared to the air gap. From the parallel plate assumption, the expected capacitances of the proposed dimensions are only a few pF. However, the parasitic capacitances increase the total capacitance. The simulations also indicate the effect of the parasitic capacitances to the total capacitance by investigating different air gap conditions. The deviations between the measured and simulated impedance values arise from the electrical devices and cables used in the measurements. Furthermore, it causes the unexpected impedances in low frequencies.

CHAPTER 5

CONCLUSION

The perforated circular MEMS membranes are designed considering effects of the perforation on the membrane behavior. The modified membrane mechanical parameters are clearly derived, and the perforation patterns are investigated. PolyMUMPs is chosen due to reliable fabricated devices found in literature. The proposed designs are fabricated with 25.6% perforation ratio. The corresponding ligament efficiency is calculated as 3/7. The membrane radius is chosen as 220 µm and 205 µm for Design A and B, respectively.

The mechanical and electrical behavior of the proposed designs are simulated by using commercially available finite element analysis package (ANSYS) and electromagnetic software (ADS & EMPro). The critical buckling stress values are simulated as -8.61 MPa and -9.36 MPa for Design A and B, respectively. For both membranes, 33.4% stress relaxation is achieved with 25.6% perforation ratio. In addition, stress relaxation produced by the perforation is simulated for the different hole radii such as 4 µm, 6 µm and 8 µm. In this way, effects of the perforation ratio on the resonance behavior of the membrane are found via linear perturbation harmonic analyses. Apart from the fabricated membranes, eight different circular membranes are simulated and compared with the analytical solutions. Minimum and maximum average percentage errors are acquired as 0.5% and 3.3% for the first vibrational mode. Furthermore, the electrical impedance values of the membranes are extracted by electromagnetic simulations.

The electrical and optical characterization of the fabricated circular MEMS membranes are performed to investigate the advantages of the perforation on the residual stress relaxation. The vibrational mode (0,1) and (0,2) of the fabricated

membranes are clearly observed under the optical measurement setup. The response of the fabricated membranes has central symmetry. The simulated vibrational mode frequencies of the membranes are in harmony with the analytical solutions and optical measurements. For the fundamental mode, the FEM results deviate 5.5% and 6.7% from the experimental work. The electrical characterizations are carried out with the impedance analyzer and results are supported by FEM.

The perforation on the membrane is used to reduce the adverse effects of the residual stress. The stress management with the perforation is succeeded and verified by the experimental work and simulations.

REFERENCES

[1] PRIME Faraday Partnership, "An Introduction to MEMS", Wolfson School of Mechanical and Manufacturing Engineering, Loughborough University, Prime Faraday Technology Watch, 2002 Loughborough University, p. 2, ISBN1-84402-020-7.

[2] K. E. Petersen, "Silicon as a mechanical material," Micromechanics MEMS Class. Semin. Pap. to 1990, vol. 70, no. 5, pp. 58–95, 1997.

[3] M. Köhler, Etching in Microsystem Technology. 1999.

[4] Bustillo, J. M., Howe, R. T., & Muller, R. S. (1998). Surface micromachining for microelectromechanical systems. Proceedings of the IEEE, Proc. IEEE, 86(8), 1552–1574. https://doi.org/10.1109/5.704260

[5] W. C. Tang, T. C. H. Nguyen, and R. T. Howe, "Laterally Driven Polysilicon Resonant Microstructures," Sensors and Actuators, vol. 20, no. 1–2, pp. 25–32, 1989.

[6] A. Sharma, D. Bansal, A. Kumar, D. Kumar, and K. Rangra, "Residual stress control during the growth and release process in gold suspended microstructures," Micromach. Microfabr. Process Technol. XIX, vol. 8973, p. 89730F, 2014.

[7] A. T. Abawi, "The Bending of Bonded Layers Due to Thermal Stress," Huges Res. Lab., vol. 1, no. 2, 2004.

[8] Hutchinson, J. W., 1996, Stresses and Failure Modes in Thin Films and Multilayers, Technical University of Denmark, Copenhagen, Denmark

[9] R. Pratap, A. Dangi, and A. R. Behera, "Effect of microfabrication induced stresses on the sensing characteristics of dynamic MEMS devices," ECS Trans., vol. 75, no. 17, pp. 35–45, 2016.

[10] A. K. Pandey, K. P. Venkatesh, and R. Pratap, "Effect of metal coating and residual stress on the resonant frequency of MEMS resonators," Sadhana - Acad. Proc. Eng. Sci., vol. 34, no. 4, pp. 651–661, 2009.

[11] B. Wagner, H. J. Quenzer, S. Hoerschelmann, T. Lisec, and M. Juerss, "Bistable microvalve with pneumatically coupled membranes," Proc. IEEE Micro Electro Mech. Syst., pp. 384–388, 1996.

[12] Ergun, A., Yaralioglu, G., & Khuri-Yakub, B., "Capacitive micromachined ultrasonic transducers," J. Acoust. Soc. Am., vol. 113, no. 3, p. 1194, 2003.

[13] L. M. Zhang, D. Uttamchandani, B. Culshaw, and P. Dobson, "Measurement of Young's modulus and internal stress in silicon microresonators using a resonant frequency technique," Meas. Sci. Technol., vol. 1, no. 12, pp. 1343–1346, 1990.

[14] R. Kamalian, Z. Ying, and A. M. Agogino, "Microfabrication and characterization of evolutionary MEMS resonators," Proc. 2005 Int. Symp. Micro-NanoMechatronics Hum. Sci. Eighth Symp. Micro- Nano-Mechatronics Information-Based Soc. - 21st Century COE Progr, vol. 2005, pp. 101–106, 2005.

[15] C. Q. Guo, Z. L. Pei, D. Fan, R. D. Liu, J. Gong, and C. Sun, "Predicting multilayer film's residual stress from its monolayers," Mater. Des., vol. 110, pp. 858–864, 2016.

[16] L. Khazanovich, S. D. Tayabji, and M. I. Darter, "Backcalculation of Layer Parameters for LTPP Test Sections, Volume I: Slab on Elastic Solid and Slab on Dense-Liquid Foundation Analysis of Rigid Pavements," Rep. No. FHWA-RD-00-086. Fed. Highw. Adm., vol. I, no. January, 2001.

[17] M. Füldner, A. Dehé, and R. Lerch, "Analytical analysis and finite element simulation of advanced membranes for silicon microphones," IEEE Sens. J., vol. 5, no. 5, pp. 857–862, 2005.

[18] Y. Tang, K. Stanley, J. Wu, D. Ghosh, and J. Zhang, "Design consideration of micro thin film solid-oxide fuel cells," J. Micromechanics Microengineering, vol. 15, no. 9, 2005.

[19] X. Lafontan et al., "Environmental test bench for reliability studies: Influence of the temperature on RF switches with metallic membranes," Des. Test, Integr. Packag. MEMS/MOEMS 2002, vol. 4755, no. April 2002, pp. 624–633, 2002.

[20] A. P. Wright, W. E. I. Wu, I. J. Oppenheim, and D. W. Greve, "Damping , Noise, and in-Plane Response of Mems Acoustic Emission Sensors," Spectrum, vol. 25, pp. 115–123, 2007.

[21] L. Li, G. Brown, and D. Uttamchandani, "Air-damped microresonators with enhanced quality factor," J. Microelectromechanical Syst., vol. 15, no. 4, pp. 822–831, 2006.

[22] R. Grixti, I. Grech, O. Casha, J. M. Darmanin, E. Gatt, and J. Micallef, "Analysis and design of an electrostatic MEMS microphone using the PolyMUMPs process," Analog Integr. Circuits Signal Process., vol. 82, no. 3, pp. 599–610, 2015.

[23] R. Grixti, I. Grech, O. Casha, J. M. Darmanin, E. Gatt, and J. Micallef, "Feasibility study of a MEMS microphone design using the PolyMUMPs process," DTIP 2014 - Symp. Des. Test, Integr. Packag. MEMS/MOEMS, no. April, pp. 1–4, 2014.

[24] A. Octavio, C. J. Martín, O. Martínez, J. Hernando, L. Gómez-Ullate, and F. M. De Espinosa, "A linear CMUT air-coupled array for NDE based on MUMPS," Proc. - IEEE Ultrason. Symp., pp. 2127–2130, 2007.

[25] A. Cowen, B. Hardy, R. Mahadevan, and S. Wilcenski, "PolyMUMPs Design Handbook a MUMPs® process," MEMSCAP Inc, 2013.

[26] S. M. Heinrich and I. Dufour, "Fundamental Theory of Resonant MEMS Devices," 2015.

[27] D. Davidovikj, J. J. Slim, S. J. Cartamil-Bueno, H. S. J. Van Der Zant, P. G. Steeneken, and W. J. Venstra, "Visualizing the Motion of Graphene Nanodrums," Nano Lett., vol. 16, no. 4, pp. 2768–2773, 2016.

[28] A. Somá and A. Ballestra, "Residual stress measurement method in MEMS microbeams using frequency shift data," J. Micromechanics Microengineering, vol. 19, no. 9, 2009.

[29] T. Uchiyama, M. Kato, and T. Yoshida, "Buckling deformation of polymer electrolyte membrane and membrane electrode assembly under humidity cycles," J. Power Sources, vol. 206, pp. 37–46, 2012.

[30] Hung M. Jo and Jo Jong Chull, "Equivalent material properties of perforated plate with triangular or square penetration pattern for dynamic analysis", Nuclear Engineering and Technology, 38, pp. 689-696, (2006).

[31] Mali Kiran Dinkar and Pravin M. Singru (2015). Vibration Analysis of Perforated Plates.

[32] R. Z. Auliya, M. R. Buyong, B. Yeop Majlis, M. F. Mohd. Razip Wee, and P. C. Ooi, "Characterization of embedded membrane in corrugated silicon microphones for high-frequency resonance applications," Microelectron. Int., vol. 36, no. 4, pp. 137–142, 2019.

[33] ANSYS, ANSYS Inc.

[34] M. Kupnik, I. O. Wygant, and B. T. Khuri-yakub, "CMUTs," pp. 487–490, 2008.

[35] M. Ghaderi, N. P. Ayerden, G. De Graaf, and R. F. Wolffenbuttel, "Minimizing stress in large area surface micromachined perforated membranes with slits," J. Micromechanics Microengineering, vol. 25, no. 7, 2015.

[36] M.A. Bozyigit, A.B. Sahin, and B. Bayram, "Design and Characterization of a Buckling-Resistant Perforated MEMS Membrane under Residual Stress", Journal of Micromechanics and Microengineering (https://doi.org/10.1088/1361-6439/ab7a7b)

[37] Keysight Technologies, "Application Note Keysight Technologies Performing Impedance Analysis with the E5061B ENA Vector Network Analyzer Introduction."